



DEGREE PROJECT IN TECHNOLOGY,
SECOND CYCLE, 30 CREDITS
STOCKHOLM, SWEDEN 2022

Sharing Quantum Resources Across a Metropolitan Network

KTH Master Thesis Report

Martin Carlnäs

Author

Martin Carlnäs <mcarlnas@kth.se>
Applied Physics
KTH, Royal Institute of Technology

Place for Project

Ericsson, Stockholm, Sweden

Examiner

Professor Val Zwiller
KTH, Royal Institute of Technology

Supervisors

Gemma Vall-Llosera - Ericsson
Samuel Gyger - KTH

Abstract

Quantum entanglement has been a popular topic amongst physicists for almost 100 years as it clearly illuminates the extreme difference between the quantum mechanical world and our classical reality. Over time, the quantum physical property of entanglement became more and more well understood and technologies utilizing entanglement are coming closer to reach industry. Quantum computers are still in the research stage but there already exists a quantum computer capable of solving tailored problems significantly faster than a classical computer. Due to algorithms like Shor's factorization algorithm and Grover's search algorithm the current cryptography schemes used to ensure secure communication risk rendering obsolete. A response to this was the invention of the **theoretically un-hackable Quantum key Distribution (QKD) scheme**, based on **generating and distributing random cryptography keys by using quantum entanglement**. To achieve this, the generation of entangled photons, or qubits, as well as detection of single photons is required. In this thesis a **Quantum Dot (QD)** is characterized and used to **generate quantum entangled states** in the Quantum Nano Photonics (QNP)-group lab at KTH as well as **sending single photons via the metropolitan fiber network** in Stockholm to Ericsson in Kista, where they are detected using **single photon detectors**. A **multi-photon emission probability of 0.049** was measured for the **exciton emission** and **0.169** for the **biexciton emission** in the KTH lab as well as a probability of **0.176** was measured for the **exciton photons** sent to Kista which is significantly **lower than the single emitter limit of 0.5** (i.e. the source is **emitting pure single photons**). Synchronization of data is of high importance in order to implement a working QKD scheme, therefore a post process temporal synchronization method based on the **biexciton-exciton cascaded decay** is implemented in the lab.

Keywords

QKD, Entanglement, SNSPD, Quantum Dot, Exciton, Biexciton

Samanfattning

Kvantsammanflätning har varit ett populärt ämne bland fysiker i snart 100 år då det tydligt belyser hur annorlunda kvantmekanikens värld är jämfört med den klassiska verklighet vi lever i. Med tiden har kvantsammanflätning blivit mer och mer välförstått och teknologier ämnade att utnyttja det har de senaste årtionden kommit allt närmare till industriell användning. Kvantdatorer är fortfarande i forskningsstadet men idag existerar det en kvantdator som kan lösa vissa problem betydligt mycket snabbare än en klassisk dator. På grund av algorithmer som Shors faktoriseringosalgoritm och Grovers sökalgoritm så riskerar dagens krypteringsprotokoll för kommunikation att bli otillräckliga. Som svar på detta har en fysikalisk icke-hackbar krypterings metodik tagits fram i form av QKD. Det baseras på att generera krypteringsnycklar från slumptal och att dessa distribueras tack vare kvantsammanflätning. För att lyckas med detta så krävs generering av sammanflätade kvanttillstånd, kvantbitar, samt singel-fotondetektorer. I den här masteruppsatsen har en kvantprick karakteriseras och används för att generera sammanflätade kvantbitar i QNP-gruppens lab på KTH samt för att skicka enstaka fotoner via Stockholms fibernät till Ericsson i Kista där de detekteras av singel foton detectorer. Multifoton sannolikheten har uppmäts till 0.049 för exciton fotoner samt 0.169 för biexciton fotoner i labbet medan ett värde på 0.176 har uppmäts för exciton fotoner detekterade hos Ericsson, vilket är betydligt lägre än singel emission gränsen 0.5 (dvs foton källan sänder ut singel fotoner). Synkronisering av data är avgörande för att få QKD att fungera varpå en post process-tidssynkroniserings metod baserad på biexciton-exciton kaskad-sönderfall har implementerats i lab.

Nyckelord

QKD, Kvantsammanflätning, SNSPD, Kvant Prick, Exciton, Biexciton

Acknowledgements

I would like to thank my main supervisor Gemma Vall Llosera and my examiner Val Zwiller for giving me the opportunity to work with this project. It has been a very fruitful learning experience as I had very little experience in applied physics or lab work in general. I am grateful that I have gotten so many resources to work with and it was fun to try and achieve something new for once. A special thanks to my second supervisor Samuel Gyger for all the help he has given me. It was a lot of fun to work close with someone who is so knowledgeable in their field. I also want to thank Thomas Lettner for all the help in the lab and discussing theoretical background as well as Jonas Almlöf for his help with the synchronization of the time-taggers.

I am also grateful for the support I have gotten outside of the work groups. I want to thank my parents, Ann-Louise Carlnäs and Torbjörn Carlnäs, as well as my brother, Carl-Henrik Carlnäs, for their support through the years and hope I can be of as much help to them as they have been to me. Lastly I would like to thank Anna Lassen for all the help and support through the years, it has been invaluable.

Acronyms

QKD	Quantum Key Distribution
DBR	Distributed Bragg Reflector
QD	Quantum Dot
SSPD	Superconducting Single Photon Detector
InGaAs	Indium Gallium Arsenide
BS	Beam Splitter
PBS	Polarizing Beam Splitter
ETA	Extensible Time Analyzer
GaAs	Gallium Arsenide
InAs	Indium Arsenide
FSS	Fine Structure Splitting
X	Exciton
XX	Biexciton
E91	Artur Ekert 1991
NF	Notch Filter
QNP	Quantum Nano Photonics
SNSPD	Superconducting Nanowire Single Photon Detector
NA	Numerical Aperture
ToF	Time of Flight
MOVPE	Metal Organic Vapor Phase Epitaxy
MMBL	Metamorphic Buffer Layer
SIL	Solid Immersion Lens
AlAs	Aluminium Arsenide
VNA	Vector Network Analyzer
PBS	Polarizing Beam Splitter
QDs	Quantum Dots
SSPDs	Superconducting Single Photon Detectors

Contents

1	Introduction	1
1.1	Background	1
1.1.1	Project Description	3
1.1.2	Related Work	3
1.2	Outline	5
2	Theoretical Background	7
2.1	Photon Statistics	7
2.1.1	Poissonian Light	8
2.1.2	Sub-Poissonian Light	8
2.1.3	Super-Poissonian Light	9
2.1.4	Second-Order Correlation	9
2.2	Quantum Dots	11
2.2.1	Quantum Structures	11
2.2.2	Entangled Single Photons	13
2.3	Superconducting Nanowire Single Photon Detectors	17
2.4	Quantum Key Distribution	18
2.4.1	Ekert Protocol from 1991	19
3	Method	21
3.1	Superconducting Nanowire Single Photon Detectors (SNSPDs)	21
3.1.1	Characterization of the Superconducting Nanowire Single Photon Detectors	21
3.1.2	Time Taggers	23
3.2	Quantum Dot	24
3.2.1	Distributed Bragg Reflector Characterization	24

CONTENTS

3.2.2	Finding and Characterizing Quantum Dots	26
3.3	Time Correlation Measurements	29
3.3.1	Second Order Correlation Measurements	29
3.3.2	Cascade Measurements	31
4	Result	34
4.1	The Quantum Dot	34
4.1.1	Photo-Luminescence Spectra	34
4.1.2	Polarization Series	35
4.1.3	Power Sweep	37
4.2	G2-Measurement	38
4.3	Cascade Measurement	41
5	Conclusion	44
References		47

Chapter 1

Introduction

1.1 Background

Almost 100 years ago the famous Einstein-Podolsky-Rosen paper was published. The paper discussed the physical property of entanglement between two quantum states as predicted by the theory of quantum mechanics. The purpose was to showcase that quantum mechanics leads to non-obvious results thus arguing that it is not a complete theory. Today quantum mechanics is an extremely well-tested theory, including all of its six building blocks, i.e. **quantization** - physical quantities of a bound system are restricted to discrete values such as energy or momenta, **wave-particle duality** - objects are described as both waves and particles. **Heisenberg's uncertainty principle** - there are upper limits in precision when making two complementary measurements such as position and momenta. **Superposition** - quantum states can be added to result in another valid quantum state. **Fragility** - a measurement on a quantum state collapses its wave-function destroying any previous information stored, and lastly **entanglement** - a sub-state of a system is not possible to describe independently of the other sub-states of the system even if separated by large distances as the states are entangled. Currently there exist devices based on quantum mechanical effects such as **semiconductor chips and lasers** and there are even technologies on the rise that can utilize quantum entanglement such as **quantum computing and quantum communication**. Quantum computing is a very hot topic and is often marketed as a solution to many high computational problems of today. Given a quantum computer with low noise and thousands of qubits, a new playing field would be opened when it comes to, for example, **simulating large physical systems**, which could be a game changer for development of new medicine and materials. However, given such a

powerful quantum computer it would also be possible to very effectively decipher any asymmetric cryptography schemes used in computing and communication today, used to ensure privacy over the internet. This includes the privacy of not just messages via email and social media but also the private accessibility to online bank accounts and other sensitive information. One of the solutions to this problem is already invented in quantum communication.

The most well known form of quantum communication is Quantum Key Distribution (QKD). It was introduced in 1984 when Bennet and Brassard introduced their protocol, BB84, for secure communication. The idea of QKD is to allow for two parties to generate keys to encrypt their messages with. These keys are generated by random numbers and each key is only used once. The combination of randomness and one-time-pad encryption makes it impossible to decipher any encrypted message. Now, how are these keys created and distributed to both parties in a secure way? By using entangled qubits (photons) the randomness is guaranteed from the statistical nature of quantum mechanics as well as the possibility to distribute the keys with an inbuilt eavesdropper detection system due to the no cloning theorem. Today there are several QKD protocols invented that all have their advantages and disadvantages. One of the earliest protocols based on entanglement was invented in 1991 by Artur Ekert, E91, and is one of the most simple forms of QKD, both in terms of implementation and comprehensibility.

To implement the E91 QKD protocol, there are some requirements that have to be met. Firstly, reliable generation of entangled single photons. Secondly, the ability to detect single photons. To implement QKD, a network is needed to transport the photons. This infrastructure already exist with the fiber networks of today, hence QKD has to be possible to integrate into these fiber networks i.e. the photons need to be in the telecom C-band or O-band. Lastly, to compare data from two parties their detection systems need to be synchronized so that they agree on temporal order of events. Today, the technology to create on demand entangled single photon pairs in the telecom C-band regime and single photon detectors capable of measuring these photon pairs exist. These are the areas to be researched during this thesis as well as a way to synchronize data between two distant parties.

1.1.1 Project Description

The goal of this project is to implement QKD in form of the Artur Ekert 1991 (E91) protocol, between the Quantum Nano Photonics (QNP) lab at KTH and Ericsson in Kista, by sending entangled qubits over a distance of 18 km through the metropolitan fiber network in Stockholm. To achieve this there are three sub-goals to be completed: i) The generation of entangled single photons from a semiconductor containing Quantum Dots (QDs) has to be examined and characterized; ii) the optical setup at KTH as well as Ericsson has to be setup to work with the wavelength the Quantum Dot (QD) emits and filter out other noise from cross-talk between fibers; and iii) characterisation and installation of two sets of commercial Superconducting Nanowire Single Photon Detectors (SNSPDs) from Single Quantum. There are two sets of detectors, one new pair that has to be characterized at KTH and another pair from 2020 that have been characterized already but has to be installed at Ericsson. The data from the detectors are recorded using time-taggers. When all of these steps are completed, second order correlation measurements will be carried out and evaluated. This is done to see what type of photon statistics the emitted photons obey and to ensure that the QD emits entangled single photons. The data recorded from two different time-taggers will have to be synchronized. This will be done by using the qubits themselves so that no extra hardware is needed to achieve synchronization. Given all these steps are solved, everything needed to implement QKD between KTH and Ericsson will be in place.

1.1.2 Related Work

As of today, there are several places in the World where QKD networks have been implemented to a varying extent. This has been done by creating entangled photons through spontaneous parametric down-conversion of a laser which results in single photon generation, however the generation of the single photons are not on demand but is instead a random process. By using a QD the single photon generation is on demand which is favourable. QKD based on single photon detection is referred to as Discrete Variable (DV)-QKD as the detection measurement is discrete, either there will be a detection event on the Superconducting Single Photon Detector (SSPD) or there will not be. While QKD based on measuring the quadratures of electrical field from the detected light (done with homodyne detectors) is referred to as Continuous Variable (CV)-QKD as the measurement outcomes are projections of the amplitude

and phase of the electrical field which are continuous [14]. In this section different works of what has been done by other groups is presented. In general, there are three things that will be highlighted. **i)** Using a single photon source in form of epitaxial semiconductor QDs, emitting two entangled photons which is required for the E91 protocol. **ii)** Synchronizing the data from two different locations by using qubits. **iii)** Implementing QKD in real world situations.

In [35] on demand generation of entangled photons in the telecom C-band has been demonstrated to show high fidelity by using two photon-resonant excitation. The photons were emitted from an epitaxial Indium Arsenide (InAs)/Gallium Arsenide (GaAs) semiconductor QD and a concurrence of 91.4% was measured as well as a fidelity of 95.2%. The multi-photon emission probability was measured to $g^2(0) = 0.038 \pm 0.005$. This is the same type of QDs used in this thesis and show great promise for single photon generation in fiber-based applications given sufficient brightness.

In [16] epitaxial InAs/GaAs semiconductor QDs were strain tuned to counteract the time-dependent state evolution of the intermediate Exciton (X) state caused by the Fine Structure Splitting (FSS). The strain tuned QDs had at most a fidelity of 90.0% with a concurrence of 87.5%.

In [24] the use of GaAs QDs excited with two photon-resonant excitation was used to implement QKD in the form of the BBM92 protocol, over the Johannes Kepler University campus in Linz. The QDs used yielded a fidelity of 98.7%, a concurrence of 95.2% and emitted photons with a wavelength at around 780 nm. The secure bit rate for the measurement was 135 bits/s with a quantum bit error rate of 1.9%. This works is similar to what is planned for this thesis, however the wavelength of the qubits here is not in the telecom C-band. The temporal synchronization was achieved by using the time delay between the X and Biexciton (XX) and was found by exploiting the strong polarization correlation between the two qubits.

The idea of using qubits to synchronize has also been used in [1] to achieve a quantum bit error rate of 0.05% for QKD run over a 26 km long fiber spool for 7 hours. It has also been suggested in [6], where they present an algorithm with low computational cost to achieve temporal synchronization by only using the hardware required for running QKD. The idea of using qubits for synchronization not only reduces the cost for QKD as less hardware is required, it also makes it more robust while not undermining the security of the QKD protocol.

[2] implemented QKD in form of a modified E91 protocol, over fiber and in open air across the Sapienza University in Rome using epitaxial GaAs semiconductor QDs excited via two photon-resonant excitation, emitting at 785 nm wavelength. They achieved a maximum fidelity of 94.3% with a multi-photon emission probability of 0.0304 and 0.0041 for the X and XX respectively for one of the QDs and 0.0045, 0.0041 for the X, XX of the other dot. Two GPS disciplined-oscillators were used to achieve the temporal synchronization of the data.

Cambridge quantum network, [9], implemented QKD over a metropolitan network using three links running BB84 protocols. The network was run for 580 days demonstrating long term stability for QKD. They used spontaneous parametric down-conversion to generate the single photons and achieved a key bit rate of 1 kilobit per second, per user.

[31] reported long-term transmission measurement of entanglement fidelity from an epitaxial InAs/GaAs semiconductor QD over a 18 km installed telecom fiber. The entanglement fidelity was recorded for seven days and measured to 91.3%. The wavelength of the X was 1329.4 nm and 1330.0 nm for the XX with detection rates of 10 kHz and 320 kHz respectively. The dot was excited below the band gap of the GaAs by so called quasi-resonant injection of carriers by using an excitation laser at 1064 nm. The anti-bunching was measured to 0.08.

1.2 Outline

In chapter 2 the theoretical background is presented to aid in the understanding of the work of this thesis. The theory behind QKD will be presented as well as the physics behind the **single photon generation and detection**.

In chapter 3 the methodology will be presented. Covering the characterization of the **Superconducting Nanowire Single Photon Detector (SNSPD)** and the QD sample as well as the correlation measurements and the processing of the data.

In chapter 4 the results for the different steps of the work will be presented with focus on the main results of the thesis, being the second order correlation measurements at Ericsson in Kista and the synchronisation of the two time-taggers to generate a Cascade plot.

CHAPTER 1. INTRODUCTION

In chapter 5 there will be some discussion regarding the different results and methods used, followed by an outlook on what is needed to achieve the end goal of the project of quantum key distribution between KTH and Ericsson.

Chapter 2

Theoretical Background

In this chapter the theoretical background is presented to aid in the understanding of the work of this thesis. Starting with a review of photon statistics for both classical and quantum light. Then covering how quantum dots can be used to create non-classical light and how a detector capable of measuring a single quanta of light is made. Ending with a discussion on a quantum light-based application, Quantum Key Distribution (QKD).

2.1 Photon Statistics

Light can be described both as a discrete stream of particles, photons, and as an electromagnetic wave. Photons are fundamental particles of light, mass-less bosons which means they do not obey Pauli's exclusion principle, making it possible to have several photons in the same quantum state. When distinguishing different types of light the quantised approach is very useful as the statistics of a light beam is used to classify different types of light. In total, there are three different photon statistics for light; Poissonian, sub-Poissonian and super-Poissonian [13]. The difference is very clear when looking at the odds of detecting n photons at a given time and comparing the probability distributions of different light given the same mean value, \bar{n} , see figure 2.1.1. All three photon statistics will be covered in this section.

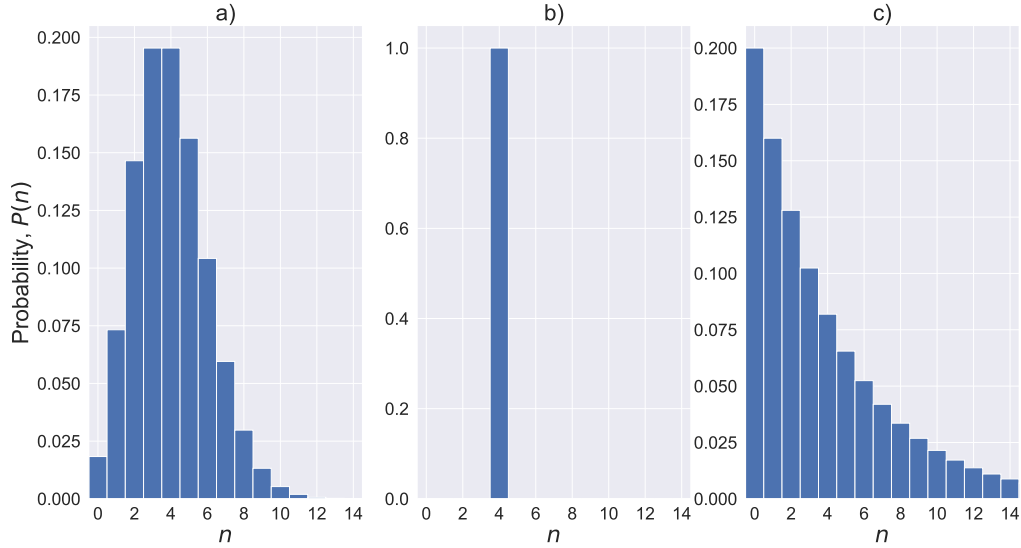


Figure 2.1.1: Probability distribution for **a)** Poissonian light **b)** sub-Poissonian light **c)** super-Poissonian light, all with a mean value of $\bar{n} = 4$.

2.1.1 Poissonian Light

Light with a Poissonian distribution is called coherent light and is what is emitted from a laser. It can be described in the second quantization as a Glauber coherent state, $|\alpha_i\rangle$, which is an eigenstate to the annihilation operator, $\mathbf{a}_i |\alpha_i\rangle = \alpha_i |\alpha_i\rangle$ [36], where

$$|\alpha_i\rangle = \sum_n |n\rangle \langle n| \alpha_i = \sum_n \exp\left(-\frac{1}{2} |\alpha_i|^2\right) \frac{\alpha_i^n}{\sqrt{n!}} |n\rangle. \quad (2.1)$$

The probability distribution is given by $P(n) = |\langle n|\alpha_i\rangle|^2 = \frac{|\alpha_i|^{2n}}{n!} e^{-|\alpha_i|^2}$ and the variance is equal to the mean photon number, $\sigma^2 = \bar{n}$, which is a characterizing property of the Poissonian distribution[13][36].

2.1.2 Sub-Poissonian Light

Sub-Poissonian light is a purely quantum optical state and does not have a classical counterpart. It is called sub-Poissonian due to the fact that the variance, $\sigma^2 < \bar{n}_i$, hence the variance is smaller for a sub-Poissonian distribution compared to a Poissonian distribution with the same mean value.

A sub-Poissonian distribution with $\sigma^2 = 0$ is a very special type of distribution, often called a photon number state or a Fock state and is an eigenstate to the number

operator $\hat{n}_i = \hat{a}_i^\dagger \hat{a}_i$. The probability distribution for a Fock state, $|n_i\rangle$, is given by

$$P(n_j) = \begin{cases} 1, & \text{for } n_i = n_j, \\ 0, & \text{for } n_i \neq n_j. \end{cases} \quad (2.2)$$

2.1.3 Super-Poissonian Light

Super-Poissonian light has a variance given by $\sigma^2 > \bar{n}$. There are two different types of super-Poissonian light, thermal light and chaotic light. Thermal light consists of a continuous spectra of oscillating modes and has a probability distribution given by $P(n) = \frac{1}{\bar{n}+1} \left(\frac{\bar{n}}{\bar{n}+1}\right)^n$, which is the Bose-Einstein distribution. Thermal light is emitted by e.g. a light bulb and the variance is given by $\sigma^2 = \bar{n} + \bar{n}^2$. Chaotic light can be found by looking at a single spectral line from a discharged lamp. Chaotic light is partially coherent and has intensity fluctuations on a time-scale similar to the coherence time [13].

2.1.4 Second-Order Correlation

In order to quantify different photon statistics the second-order correlation function $g^2(\tau)$ is a very useful tool. It is defined as

$$g^2(\tau) = \frac{\langle E^*(t)E^*(t+\tau)E(t+\tau)E(t)\rangle}{\langle E^*(t)E(t)\rangle \langle E^*(t+\tau)E(t+\tau)\rangle} = \frac{\langle I(t)I(t+\tau)\rangle}{\langle I(t)\rangle \langle I(t+\tau)\rangle}, \quad (2.3)$$

where $\langle \dots \rangle$ is a temporal average over a long time period, $E(t)$ is the electrical field and $I(t)$ is the intensity of the light [13]. The value of the $g^2(\tau)$ gives a measure of how likely it is to detect a photon within time τ after another when looking at a light beam. A value of 1 corresponds to uncorrelated photons meaning the detection events are completely unrelated.

In the second quantization the electrical fields can be written as $E_k(t) = E_k^+(t) + E_k^-(t)$ where

$$\begin{aligned} E_k^-(t) &\sim a_k \cdot \exp(-i\omega_k t) \\ E_k^+(t) &\sim a_k^\dagger \cdot \exp(i\omega_k t), \end{aligned} \quad (2.4)$$

which results in the correlation function

$$g^2(\tau) = \frac{\langle E_k^-(t)E_k^-(t+\tau)E_k^+(t+\tau)E_k^+(t)\rangle}{\langle E_k^-(t)E_k^+(t)\rangle^2}. \quad (2.5)$$

Using the commutation relation for the annihilation and creation operators $[a_i, a_j^\dagger] = \delta_{ij}$ and letting $\tau \rightarrow 0$, the correlation function can be written as, [25],

$$g^2(0) = \frac{\langle a_k^\dagger a_k^\dagger a_k a_k \rangle}{\langle a_k^\dagger a_k \rangle^2} = \frac{\langle n(n-1) \rangle}{\langle n \rangle^2} = \frac{\langle n^2 \rangle - \langle n \rangle}{\langle n \rangle^2} = 1 + \frac{\sigma^2 - \langle n \rangle}{\langle n \rangle^2}. \quad (2.6)$$

It should now be clear that the correlation function will be depending on the photon statistics of the light beam as it is proportional to the variance of the photon statistics.

For Poissonian light the variance is equal to the mean value resulting in $g^2(0) = 1$. Thus a coherent light source has completely uncorrelated photons and the temporal difference between photons is truly random [36].

Sub-Poissonian light has a variance $\sigma^2 < \langle n \rangle$, resulting in

$$g^2(0) = 1 + \frac{\sigma^2 - \langle n \rangle}{\langle n \rangle^2} < 1. \quad (2.7)$$

This means that the photons are *anti bunched*, that is, it is less likely to detect two photons simultaneously. For a light beam emitted from a single photon source, Fock state with $n = 1$, the variance is 0 and the mean value is 1 resulting in $g^2(0) = 0$, thus for a true single photon source there will never be multiple photon events at once. For a light beam emitted from multiple single photons sources or a Fock state with $n > 1$, the second-order correlation function is $g^2(0) = 1 - \frac{1}{n}$, since $\langle n \rangle = n$ for Fock states. Hence, the $g^2(0)$ is a good measurement to evaluate purity of a single photon emitter [36].

For super-Poissonian light, the variance is larger than the mean value which results in $g^2(0) > 1$. This means that the photons are experiencing *bunching*, meaning it is more likely to detect multiple photons at the same time. For thermal light specifically the variance $\sigma^2 = \langle n^2 \rangle + \langle n \rangle$ and hence $g^2(0) = 2$ [13].

2.2 Quantum Dots

As mentioned in the previous section, sub-Poissonian light is a quantum optical phenomenon. Currently, there are two common ways to achieve such photon statistics. Either by letting a strongly attenuated laser beam undergo a non-linear process or using a quantum system, e.g. traps in semiconductors where there is a single photon emitted from a transition from an excited state to a ground state level [36]. In this section the generation of single photons emitted from a quantum system will be covered.

2.2.1 Quantum Structures

In nano-structures there are physical effects that occur due to quantum confinement. This is a result from Heisenberg's uncertainty principle, where the uncertainty in momentum space, Δp_i , is dependent on the uncertainty of the position space, Δq_i , by the following relation, $\Delta p_i \Delta q_i \geq \frac{\hbar}{2}$, where $i = x, y, z$. For a massive particle with mass, m , a confinement in position space, Δq_i , will contribute to the particle's kinetic energy,

$$E_{confinement,i} = \frac{(\Delta p_i)^2}{2m} \geq \frac{\hbar^2}{8m(\Delta q_i)^2}. \quad (2.8)$$

Comparing with the thermal energy, $E_{thermal} = \frac{1}{2}k_B T$, the confinement, Δq_i , will be significant if $\Delta q_i \leq \sqrt{\frac{\hbar^2}{mk_B T}}$. Assuming an electron with mass m_e and a temperature at $\sim 10K$, this corresponds to a confinement $\Delta q_i \lesssim 9.4$ nm, hence confinement effect has to be considered when dealing with nano-structures [12].

Depending on the number of dimensions that experience confinement different physics apply due to change in energy and density of state. In a bulk semi-conductor, holes and electrons are able to move freely in all three directions within their respective bands. Hence, they experience 3-D physics. If one dimension experience quantum confinement the charged carriers are said to be located in a quantum well and thus 2-D physics apply. Confinement in two directions imply 1-D physics and is referred to as quantum wire. Lastly, quantum confinement in all three directions creates a completely quantized motion for the charged carriers that experience 0-D physics in what is called a QD [12]. The density of state for a quantum dot is completely discrete which is why QDs commonly are referred to as *artificial atoms* and a lot of the morphology regarding QDs is adopted from atoms. When talking about the energy

levels of carriers one refers to them as shells, the s-shell being the lowest and the p-shell the second to lowest [25].

How a semi-conductor is made to contain epitaxial QDs is a large field and a detailed treatment is beyond the scope of this thesis. The interested reader is referred to [20]. Instead a quick presentation of the sample used will be done here and for a more in depth description of the process and all its intricacies see [22] for the quantum dots used in this thesis.

Epitaxial Quantum Dots

A semiconductor host matrix houses epitaxial quantum dots. Three-dimensional confinement is achieved by mixing two different band-gap semiconductors locally. The quantum dots used in this thesis are made of InAs within a Indium Gallium Arsenide (InGaAs) host and are grown using Metal Organic Vapor Phase Epitaxy (MOVPE). The InAs is located on top of a Metamorphic Buffer Layer (MMBL) consisting of InGaAs with an increasing amount of Indium to reduce the strain on the InAs film, which allows for emission in the telecom C-band [22]. Photons are emitted in arbitrary directions from a QD. This is not a desirable trait so to counteract this a so called Distributed Bragg Reflector (DBR) is located underneath the MMBL. A DBR acts as a mirror and is made of a stack of two different types of semiconductors with alternating high refractive indices materials, Aluminium Arsenide (AlAs) and GaAs in this case. It achieves reflection by constructive interference at desired wavelengths. In order to generate cumulative constructive interference from the reflected light at each interface of the layers, the phase difference, $\Delta\Phi = \frac{2\pi}{\lambda} \cdot d\lambda$, must be $n \cdot \lambda$, where $n \in \mathcal{N}$ for one of the two semiconductor layers in the stack. Hence, the optical thickness, $d \cdot \lambda$, has to be $1/4 \cdot \lambda$, i.e. the thickness of each layer of the stack must be $d_i = \frac{\lambda}{4n_i}$ where i indicates which of the two types of semiconductor the layer is made of [22]. See figure 2.2.1 for a graphical representation of the wafer structure.

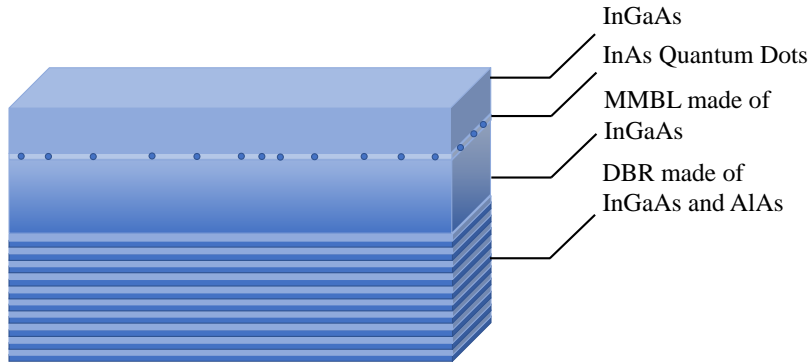


Figure 2.2.1: Schematic of the wafer structure including the QDs, MMBL, DBR and the InGaAs cap.

2.2.2 Entangled Single Photons

Entanglement

The notion of entanglement was first introduced in an attempt to disprove quantum mechanics by Einstein, Podolsky and Rosen in 1935. They believed that it was a nonphysical result of quantum mechanics and Einstein even referred to it as "spooky action at a distance" [10]. Today it is a well known phenomenon and of interest in a lot of new technologies e.g. quantum communication [8][29] and quantum information [11][3]. A multi-particle state $|\Psi\rangle$ is said to be entangled if it is not possible to factorize it as a product state, $|\Psi\rangle = |\Psi_A\rangle \otimes |\Psi_B\rangle$, where A and B indicates two sub-states [13]. Entanglement is not an absolute entity but can manifest in various degrees. Taking two photons as an example, they can be entangled in time, path or polarization. The polarization will be in focus here and is typically expressed in three different bases, linear basis (*horizontal* $|H\rangle$ and *vertical* $|V\rangle$), diagonal basis (*diagonal* $|D\rangle$ and *anti-diagonal* $|A\rangle$) and circular basis (*right* $|R\rangle$ and *left* $|L\rangle$). For the two photon state, there are several different possible states that are entangled but some of them are so called maximally entangled states. This means that they are perfectly correlated independent of basis. There are four specific maximally entangled states called Bell States. These states make up a orthonormal basis for the four dimensional Hilbert space (vector space with an inner product that is symmetric, linear and positive-definite) of the photons polarization. Looking at the photons in the linear basis there four bell states

can be written

$$|\Psi\rangle = \begin{cases} |H, H\rangle \pm |V, V\rangle, \\ |H, V\rangle \pm |V, H\rangle. \end{cases} \quad (2.9)$$

A polarization measurement made on one of the photons in any of the above states in equation 2.9 would also give the polarization of the second photon. This is not only true for measurements in the linear basis but for any complementary basis, diagonal or circular, as the photons are maximally entangled [7].

Exciton and Biexciton

When an electron inside the valence band of a QD is excited into a higher energy state, a hole with opposite spin is created in the valence band. A electron in the conduction band can bind to such a hole through their mutual Coulomb interaction to form a quasi-particle called an Exciton (X) [18]. There are different excitation paths that create excitons, above band gap excitation or exciting a electron directly into one of the lower energy levels (shells). For p-shell excitation the electron is excited to the p-shell and then quickly relax, $\sim 10^{-13}$ s, into the s-shell [12]. Using p-shell excitation is often beneficial for optical performance and is what was used in this thesis [25]. There are four possible combinations of the exciton state, with different spin configurations; $|X\rangle = |\uparrow_e \downarrow_h\rangle$, $|X\rangle = |\downarrow_e \uparrow_h\rangle$ and the superposition states $|X\rangle = \frac{1}{\sqrt{2}} (|\uparrow_e \downarrow_h\rangle + |\downarrow_e \uparrow_h\rangle)$ and $|X\rangle = \frac{1}{\sqrt{2}} (|\uparrow_e \downarrow_h\rangle - |\downarrow_e \uparrow_h\rangle)$. The lifetime of an exciton is in the ns range and it ends when the electron de-excites down into the valence band via photon emission. There is also a possibility that it de-excites via a non radiative process.

Similar to the exciton is the Biexciton (XX), which is a quasi particle consisting of two electron-hole pairs that experience additional binding energy compared to two separate X. There is also the possibility to have two electrons paired with one hole or one electron paired with two holes, each of these quasi particles are called a Trion (T). See figure 2.2.2 for a graphical representation of the three quasi particles.

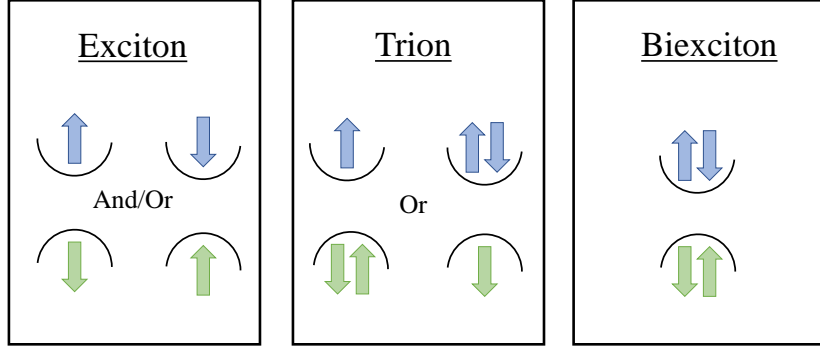


Figure 2.2.2: Blue arrows represent the spin of the electrons and green arrows represent the spin of the holes.

Fine Structure Splitting

Unlike the exciton, the biexciton cannot transition directly into the ground state but rather has to do a cascaded biexciton-exciton decay, see figure 2.2.3. To understand this process, a look into the spin to spin interaction is required. The total angular momentum $J = L + S$, for electrons is equal to its spin, $J_e = S_e = \frac{1}{2}$, as the angular momentum $L_e = 0$, while for holes $L_h = 1$ and $S_h = \frac{1}{2}$, resulting in three different total angular momenta. Only heavy holes, i.e. holes with $J_h = \frac{3}{2}$ and $J_{h,z} = \pm \frac{3}{2}$ are considered in this thesis. The total angular momentum for an optically active exciton is $J_X = \pm 1$. The interaction energy for re-combination of an X is given by the following Hamiltonian, $\mathcal{H}_{Exchange} = - \sum_i (a_i J_{h,i} S_{e,i} + b_i J_{h,i}^3 S_{e,i})$ with $i = x, y, z$ where $J_{h,i}$ and $S_{e,i}$ represent the total angular momentum in i for the hole and electron respectively, and a_i and b_i characterize the interaction strength of the spins. The value of $\mathcal{H}_{Exchange}$ depends on several factors, hole type in the X, symmetry, crystal structure and orientation as well as strain in the QD [25][36]. For an exciton with known spin, the energy level is two fold degenerate due to the Pauli principle. When the biexciton decays into the exciton state it can do so in two ways, as it consists of two electron-hole pairs see figure 2.2.3. The energy difference for the two possible super-positioned exciton states, ($|X\rangle = \frac{1}{\sqrt{2}} (|\uparrow_e \downarrow_h\rangle + |\downarrow_e \uparrow_h\rangle)$ and $|X\rangle = \frac{1}{\sqrt{2}} (|\uparrow_e \downarrow_h\rangle - |\downarrow_e \uparrow_h\rangle)$) is called the Fine Structure Splitting (FSS) and can be up to several hundreds of μeV . For a degenerate state the FSS, $\delta_{FSS} = 0$, i.e. the energy levels in figure 2.2.3b for the two X states are equal.

For a biexciton-exciton decay with zero FSS, the XX can transition into the X state by emitting a photon with either left- or right-circular polarization. When the X state decays into the ground state, a photon with opposite polarization is emitted, i.e. right-

or left-circular polarization as shown in figure 2.2.3b [25]. The absence of FSS makes the two decay paths indistinguishable in wavelength. If no information about the lights polarization is available, the two photon state can be written as a superposition

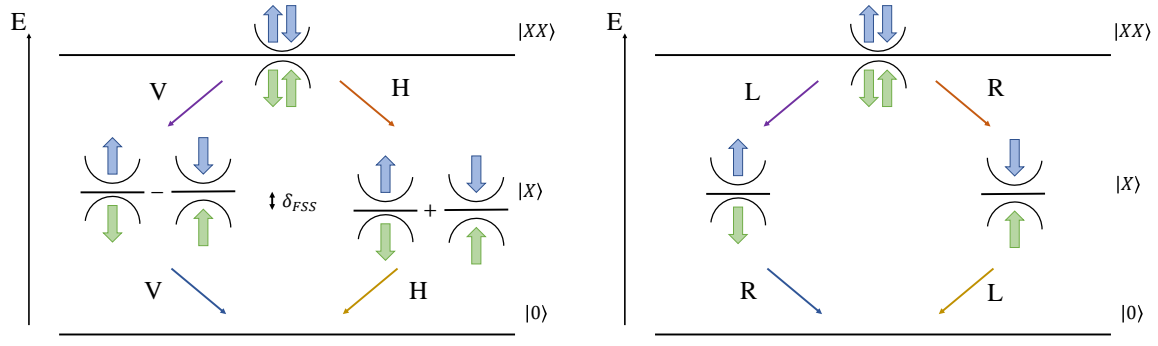
$$|\Psi\rangle = \frac{1}{\sqrt{2}} (|L_{XX}R_X\rangle + |R_{XX}L_X\rangle) = \frac{1}{\sqrt{2}} (|H_{XX}H_X\rangle + |V_{XX}V_X\rangle), \quad (2.10)$$

where $|L_i\rangle = \frac{1}{\sqrt{2}} (|H_i\rangle + i|V_i\rangle)$ and $|R_i\rangle = \frac{1}{\sqrt{2}} (|H_i\rangle - i|V_i\rangle)$ [25]. Hence, the two photons are maximally entangled.

The biexciton-exciton cascade with a FSS, $\delta_{FSS} > 0$ the two X states are non-degenerate and there is now a difference in photon energy for the two transition paths that make them distinguishable. This results in a time dependency between the two photons emitted from the cascaded decay and the light state can be written as

$$|\Psi\rangle = \frac{1}{\sqrt{2}} \left(|H_{XX}H_X\rangle + e^{\frac{i\delta_{FSS}}{\hbar}t} |V_{XX}V_X\rangle \right). \quad (2.11)$$

Even though there is a time dependent phase between the horizontal and vertical decay paths the two sates emitted from a biexciton-exciton cascade experiencing a FSS between its two X states, the two photons are still in a maximally entangled state [36].



(a) Shows the biexciton-exciton cascade with FSS, $\delta_{FSS} > 0$.

(b) Shows the biexciton-exciton cascade with no FSS, $\delta_{FSS} = 0$.

Figure 2.2.3: Blue arrows represent the spin of the electrons and green arrows represent the spin of the holes. In both of the figures the polarization of the photons is known.

2.3 Superconducting Nanowire Single Photon Detectors

In 1971 it was demonstrated that laser light could break the superconductivity of Pb films and that this was not due to thermal effects [28]. Since then a lot of research has been made on Superconducting Single Photon Detectors (SSPDs) of different kinds and today one of the most promising types of detectors are the Superconducting Nanowire Single Photon Detectors [21]. The general idea of the SNSPD is outlined in figure 2.3.1.

i) The nanowire is kept below its critical temperature, T_c , and has a direct current biased below its critical current, I_c . **ii)** The absorption of a photon creates a local hotspot by disrupting Cooper pairs in the nanowire. This local hotspot is no longer superconducting. **iii)** The local hotspot forces the current to flow through a smaller cross-section which makes the current surpass the critical current. **iv)** The wire is no longer superconducting and a resistance is created in the wire. This rapid increase in resistance gives rise to a voltage spike that can be measured. **v)** The nanowire is heated up through resistive heating which creates a resistive barrier across the nanowire. **vi)** The nanowire is cooled down below its critical temperature once more by its cryogenic environment and returns to state **i)** [21].

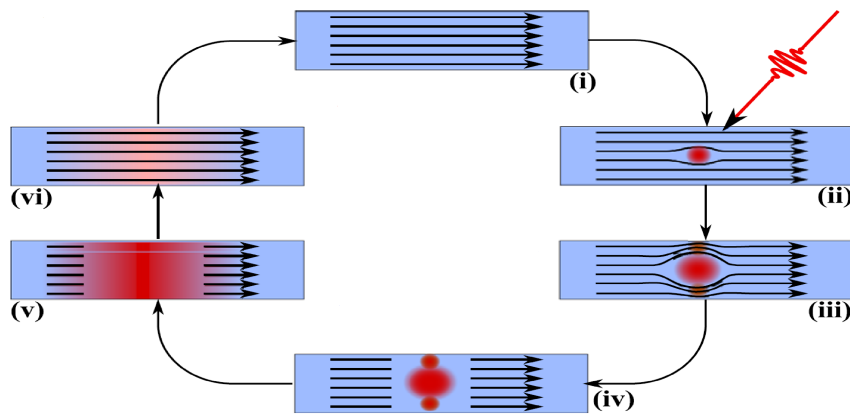


Figure 2.3.1: **i)** The nanowire is in its superconducting state. **ii)** The absorption of a photon creates a local hotspot. **iii)** The current is forced to flow through a smaller cross-section. **iv)** The smaller flow through the smaller cross-section surpasses the critical current. This gives rise to resistance across the wire and a voltage spike can be measured. **v)** The presence of resistance causes resistive heating in the wire creating a resistive barrier across the nanowire. **vi)** The nanowire is cooled down by its cryogenic environment and returns to its superconducting state. Image is modified from [21].

Today SNSPDs are widely used due to their high efficiency, low time jitter, short dead time and low dark counts [21][27][33]. Photons in the visible and infrared regime can be detected using SNSPDs. The time between **v**) and **i**) in figure 2.3.1 is referred to as the dead-time as the SNSPD is unable to detect any photons in this time-frame. Today the dead-time for SNSPDs can be made less than 10 ns [15]. The efficiency of SNSPDs have been measured to be as high as 98% [23]. The time jitter is the precision in time measurement and detectors with a time jitter lower than 10 ps exist [34]. A dark count refers to a detection event on the SNSPD that is not caused by an intended photon. This could be thermal radiation, background noise in the fiber connected to the SNSPD or a fluctuation in the biased current over the detectors. The dark count level for a SNSPD can be kept at a quite low rate of 30 dark counts per second [36]. It should be mentioned that the efficiency and dark counts are both dependent on the current biased over the nanowire. The efficiency is higher when having a bias current close to the critical current as the sensitivity increases but this also results in more dark counts.

2.4 Quantum Key Distribution

Secure online communication is today achieved by using classical encryption, which typically uses products of large prime numbers to encrypt messages as a classical computer requires a lot of computation time to factorize out the primes. However, for a quantum computer this would not be nearly as time consuming as the use of Shor's algorithm allows for polynomial factorization of prime numbers instead of exponential, as for classical computers [26]. If quantum computers will be as powerful tools as researchers hope, a new way to encrypt online messages is needed. By using a completely randomized key the deciphering of encrypted messages would be difficult even for a quantum computer. However, if the key is used multiple times, patterns could be found making it possible to decipher. To counteract this so called one-time-pad protocols have been introduced, suggesting to generate a new key for each message. Encryption using truly randomized keys with a one-time-pad protocol would be impossible to decipher and this is where quantum cryptography enters.

The first invention of quantum cryptography is from 1984 when Bennet and Brassard introduced their famous BB84 protocol. The idea of the BB84 protocol is to use quantum bits to distribute a secure key between two parties, typically named Alice and Bob, that can be used to encrypt messages between them, this type of cryptographic protocol is called Quantum Key Distribution (QKD). It is secure in the sense that it is able to detect if there is an eavesdropper, typically named Eve, that has listened in when Alice and Bob shared their key. This is based on the famous no cloning theorem, [30], from 1982 that proves that it is impossible make a perfect clone of an arbitrary quantum state. Today there are several QKD protocols that have been invented and the one invented by Ekert in 1991 is in focus in this thesis.

2.4.1 Ekert Protocol from 1991

In 1991 Arthur Ekert published his quantum protocol for QKD known as the E91 protocol. The protocol is based on using two maximally entangled photons and the fact that they are correlated regardless of basis choice [11].

E91 protocol

A single photon source generates two maximally entangled photons, for example the state $|\Psi\rangle = \frac{1}{\sqrt{2}} (|H_A H_B\rangle + |V_A V_B\rangle)$. Alice receives one photon (qubit) and Bob receives the other. Alice measures the polarization of the received photon in either the linear- or diagonal-basis and records the measured polarization as well as the choice of basis. Bob does the same with his received photons. After the measurements are done they share their choice of basis over an open communication line, this gives no information about their measured values. For all measurements done in the same basis the two photons will be completely aligned, these measurements will be used for generating the key. The measurements done in different bases will be ignored, see figure 2.4.1.

Alice:	<table border="1" style="width: 100%; border-collapse: collapse;"> <tr> <td style="padding: 2px;">Basis</td><td style="text-align: center; padding: 2px;"></td></tr> <tr> <td style="padding: 2px;">Result</td><td style="text-align: center; padding: 2px;">D V V A H A D V A A V D H V</td></tr> </table>	Basis		Result	D V V A H A D V A A V D H V
Basis					
Result	D V V A H A D V A A V D H V				
Bob:	<table border="1" style="width: 100%; border-collapse: collapse;"> <tr> <td style="padding: 2px;">Basis</td><td style="text-align: center; padding: 2px;"></td></tr> <tr> <td style="padding: 2px;">Result</td><td style="text-align: center; padding: 2px;">D D V A H H D V H A V D H D</td></tr> </table>	Basis		Result	D D V A H H D V H A V D H D
Basis					
Result	D D V A H H D V H A V D H D				
Key:	1 - 0 0 1 - 1 0 - 0 0 1 1 -				

Figure 2.4.1: Shows an example of the E91 protocol where 14 measurements were done by Alice and Bob. Here polarization D and H corresponds to 1 and polarization V and A corresponds to 0. The bell state used in this example was $|\Psi\rangle = \frac{1}{\sqrt{2}}(|H_A H_B\rangle + |V_A V_B\rangle)$.

If an eavesdropper, Eve, were to intercept one of the photons and measure them, she would have to perfectly guess the correct choice of basis of the intended receiver. The odds of this are $(\frac{1}{2})^N$, where N is the number of measurements Alice and Bob measured in the same basis. For each measurement she does not guess the basis correctly, she has to guess the polarization in the complementary basis, i.e. also a 50/50 chance to get it right, this is all due to the fact that the no cloning theorem prevents Eve from making a copy of the original state. Hence, if Eve were to intercept one of the receivers photons, Alice and Bob would in some cases measure different polarization even when their choice of basis was the same. To check if this is the case either Alice (or Bob) can sacrifice random parts of her key and share it on a public channel so that the Bob (or Alice) can compare with his (or hers) key. If no eavesdropper interfered, the two keys will be identical, hence Alice and Bob can now safely encrypt their messages. If the keys do not match, Alice and Bob know that someone has eavesdropped.

Chapter 3

Method

In this chapter the experimental steps will be covered. Starting at the detection end with the SNSPDs, moving on to the source, the QD, and finally going through the g^2 - and cascade measurements and how the data measured is processed.

3.1 Superconducting Nanowire Single Photon Detectors (SNSPDs)

Two sets of detectors from Single Quantum are used in this project, one set from year 2020 and the other from 2021. The 2020 detectors have an efficiency of $\sim 30\%$ with a time jitter below 95 ps. The other detectors arrived in the beginning of the project (2021) and had to be characterized for 1550 nm, see below. The 2020 detectors were installed in Ericsson's lab in Kista and the new detectors were installed in the QNP lab at KTH.

3.1.1 Characterization of the Superconducting Nanowire Single Photon Detectors

The new SNSPDs at KTH were characterized to test the efficiency and the dark counts at different bias currents. This was done by using a highly attenuated laser at $\lambda = 1550 \text{ nm}$ connected to the detectors while varying the bias current over the detectors, see figure 3.1.3 for a schematic. To get the efficiency, the power at the end of the setup, E_{ref} , was measured with a power meter and then compared to the amount of counts, n , detected

by the SNSPDs by using $E_{tot} = \frac{h \cdot c}{\lambda} \cdot n$. The efficiency then corresponds to $\eta = \frac{E_{tot}}{E_{ref}}$. To measure the dark counts, the detection events were recorded while varying the bias current without having any light source connected to the detectors. In figure 3.1.1 the results of the efficiency and the dark counts are plotted. There is a balance between high efficiency and dark counts when choosing the bias current as both the efficiency and dark counts increase with the bias current. For example, to get as high efficiency as possible with low dark count rate, a bias current of 15 μ A for detector 2 would be good as the dark counts are close to zero while the efficiency is still $\sim 50\%$.

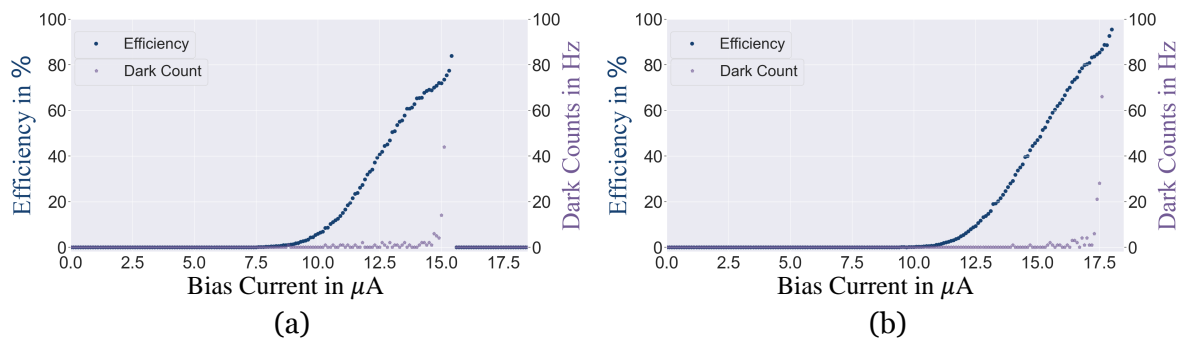


Figure 3.1.1: Shows the efficiency and the dark counts for the two detectors at different bias current. **a)** Detector 1 with a critical current $I_{crit} = 15.4 \mu\text{A}$. **b)** Detector 2 with a critical current $I_{crit} = 18.0 \mu\text{A}$.

To measure the uncertainty in time, *time jitter*, an attenuated 80 MHz laser, *APE PicoEmerald 1*, was put in front of the detectors and the detection events from the SNSPDs were recorded by a *Waverunner 640zi* oscilloscope, generating a Time of Flight (ToF) histogram for each detector. Taking the full width half max of the ToF histogram on the oscilloscope gives the time jitter for the entire setup. The entire system's time jitter can be written as $\epsilon_{system} = \sqrt{\sum_i \epsilon_i^2}$, where ϵ_i corresponds to each component in the setup, in this case the laser, the SNSPD and the oscilloscope. Both the oscilloscope and laser have very low time jitter, each having only a few ps. While the time jitter for the SNSPD is in the order of tens of ps. Hence, the main contribution to the system's time jitter comes from the SNSPD and the measured value acts as rough approximation. The time jitter measured for detector 1 was < 47.2 ps, see figure 3.1.2a and for detector 2 the time jitter was < 21.1 ps, see figure 3.1.2b.

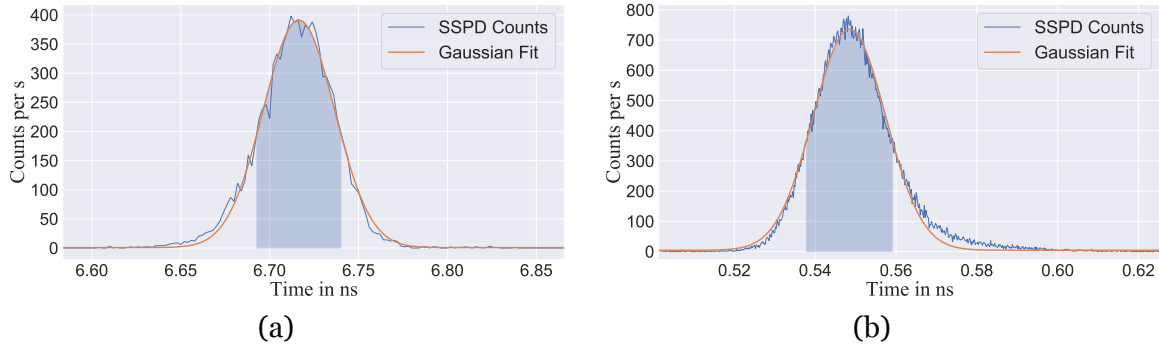


Figure 3.1.2: **a)** From the full width half max of the fitted normal distribution a time-jitter of 47.2 ps is retrieved for detector 1. **b)** From the full width half max of the fitted normal distribution a time-jitter of 21.1 ps is retrieved for detector 2.

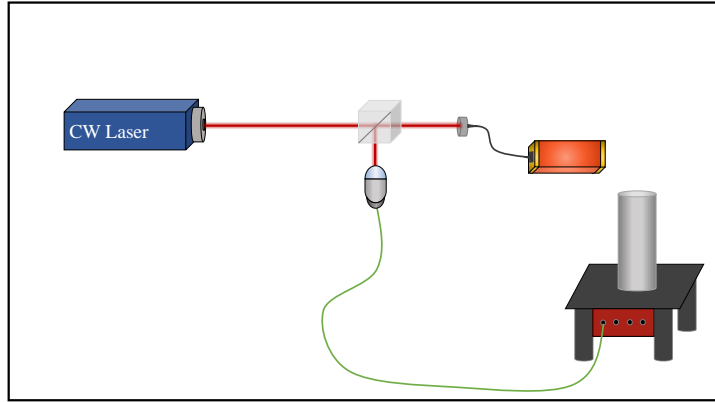


Figure 3.1.3: Optical setup for the SNSPD characterization. A highly attenuated continuous-wave laser at 1550 nm wavelength is split by a beam splitter, one arm going to the detectors and the other on a powermeter. A legend for all the optical equipment used in this figure can be found in figure 3.2.2a.

3.1.2 Time Taggers

A Time tagger is a high precision time-to-digital converting device that is used to record the detection events from the SNSPDs and store them on a computer. They convert the pulse in voltage from the detectors and stores them into a data file with a time stamp. These files can than be used to create ToF histograms for the g^2 - and cascade measurements. In order to process the data files created, a software called Extensible Time Analyzer (ETA) was used [19]. It was made by the QNP group and is a convenient way to cope with the data as ETA runs in C but allows the user to use graphical and python interfaces.

QuTAG

The time taggers, QuTAG, used in this project were bought from quTools. The QuTAG has one start and four stop channels available with a time resolution of 1 ps and a time jitter smaller than 10 ps RMS. It stores the detection event as a time stamp in absolute time and to retrieve a time difference between two detection events post processing is required. A 10 MHz reference signal can be connected to ensure that the QuTAG's time does not drift away in time.

3.2 Quantum Dot

A big challenge with implementing QKD in real world environments is that it needs to be integrated into the current infrastructure i.e. footprint and power consumption needs to be manageable, volume cost needs to be available and, if going through fiber, light emission needs to be in the telecom C-band.

There are different methods for generating single photons in the 1550 nm range, either by using a highly attenuated laser or, as used in this project, a QD. The advantages of using a QD, Fock state, over an attenuated laser, coherent state, is that the photon statistics are different, as seen in chapter 2, and also that the QD can generate an entangled photon pair. However, to use such a dot, one needs to grow a wafer sample and locate a bright QD from it, that can generate two entangled photons, with low FSS, as there are no such QDs that are available to purchase off-the-shelf. In this section the process of finding such a dot will be covered, starting with characterizing the DBR to get a dot that is as bright as possible, then going over the probing of the sample to locate a suitable dot and how to characterize its properties.

3.2.1 Distributed Bragg Reflector Characterization

The wafer sample 8366 is a III-V semiconductor that was grown at KTH, in Kista by the group of Prof. Matthias Hammar, see [22] for how the sample was made. A graphical illustration of the sample is found in 2.2.1. In order to find a bright dot, the DBR of the wafer was characterized so that a part of the sample with high reflection at the target wavelength of 1550 nm could be used. This was done by dividing the wafer into different same size regions, see figure 3.2.1, then comparing, region by region, the spectrum of a *Halogen Light Source HL-2000* reflected from the DBR to

the spectrum reflected by a mirror. See figure 3.2.2b for a schematic of the setup. The spectrometer used for these measurements was a *NIRquest Ocean Optics Near infrared Spectrometer*.

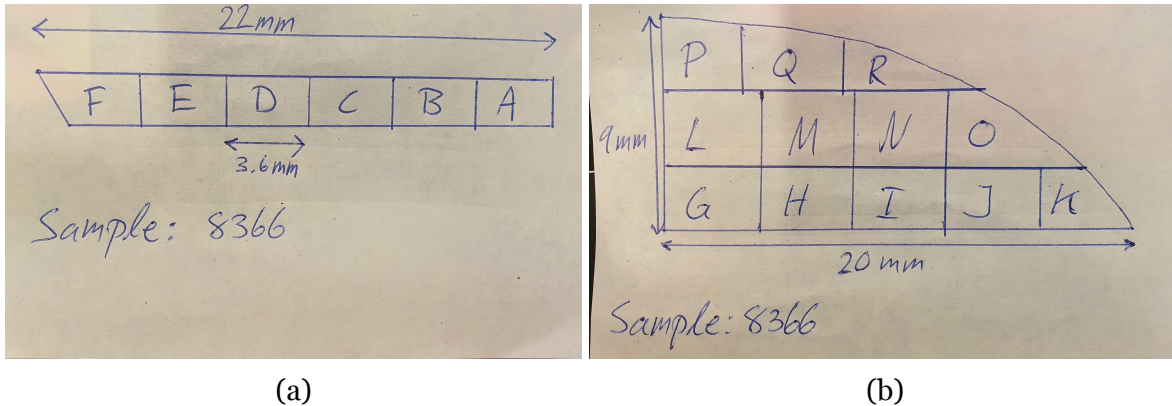


Figure 3.2.1: Illustrates the regions of two parts of wafer sample 8366 with the characterized regions marked. **a)** Show region A-F for sample 8366. **b)** Shows region G-P for sample 8366.

Optical Setup

In figure 3.2.2a all the different optical elements and all the equipment used in all of the different schematics of different setups are listed.

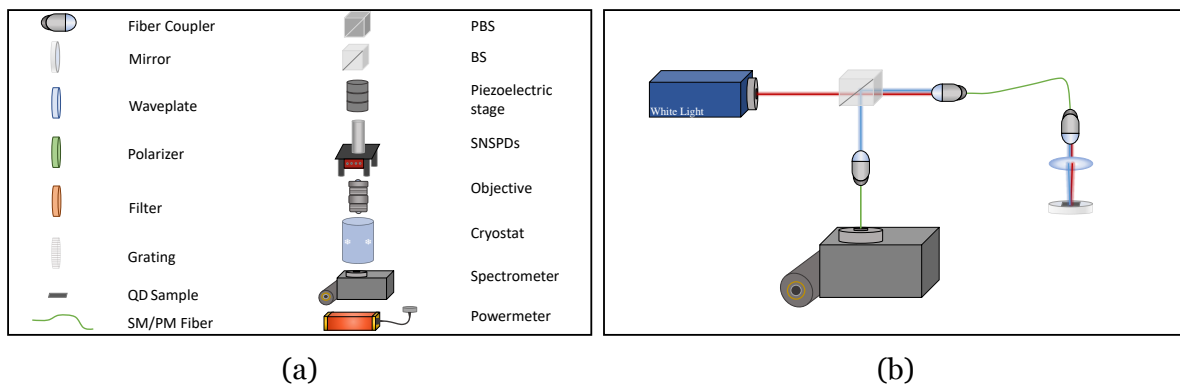


Figure 3.2.2: **a)** Different equipment used in the setups. **b)** Optical setup for DBR characterization. The light is split by a 90/10 beam splitter, focused through a lens and reflected off the mirror/sample, collimated into the fiber coupler and finally reflected by the beam splitter again and detected by the spectrometer.

The region chosen to use was part C of the sample and in figure 3.2.3 the spectrum reflected off the background and part C is shown. The spectra of the other regions of the sample are found in the appendix A.1.

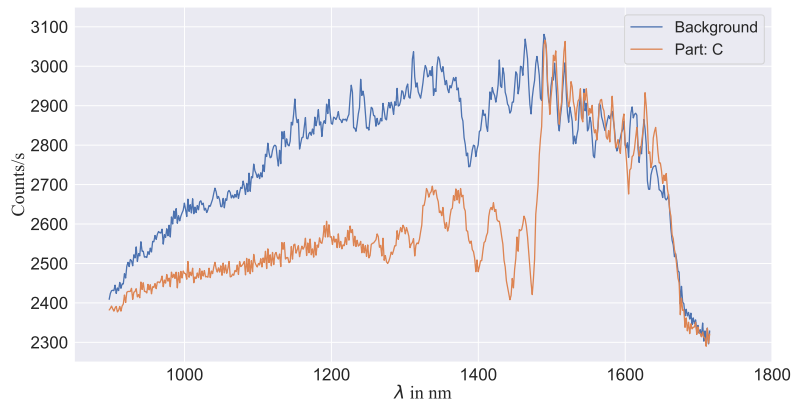


Figure 3.2.3: In this figure the reflected light of region C of sample 8366 is compared to the spectra reflected of the mirror.

3.2.2 Finding and Characterizing Quantum Dots

The setup for finding and characterizing the quantum dots is shown in figure 3.2.4a and figure 3.2.4b. The laser passes through a polarizer that filters all but the H-polarisation, a motorized half-waveplate that rotates the polarization and another polarizer, also only letting horizontally polarized light through. This makes it possible to control the power of the laser beam without having to tune the laser itself.

After this combination the polarised light is then split up by a 90/10 Beam Splitter (BS) where 90% of the beam goes to the powermeter and 10% of the beam goes into the objective inside the cryostat. The objective has a Numerical Aperture (NA) of 0.8 and the laser is focused on the sample in a spot with $\sim 2 \mu\text{m}$ in diameter. The same area is where the single photons emitted from the QDs are collected alongside the reflected laser light. The single photons and the laser then pass through the objective and hit the BS once again. Afterwards the laser is filtered out by a long-pass filter. Finally the single photons pass through a polarizer, a motorized half waveplate and a Polarizing Beam Splitter (PBS) before being detected by the spectrometer.

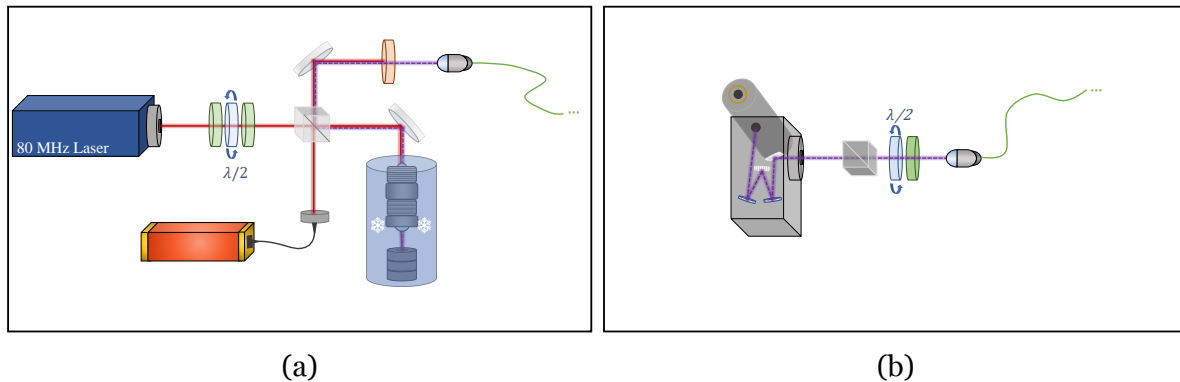


Figure 3.2.4: **a)** Optical setup for the excitation of the QDs. The 80 MHz pulsed tunable laser is sent through a polarizer, a motorized half-waveplate followed by another polarizer. The light is then split by a 90/10 BS where 90% of the light is sent to a powermeter and the other 10% is coupled to the cryostat where it is focused with an objective on the QD sample. The light emitted from the dot and the reflected laser beam are coupled back through the objective and reflected off the BS. Thereafter the light beam passes through a long-pass filter where only the QD emission passes through and is then coupled into a fiber. **b)** Optical setup for the characterization of the dot on the spectrometer. The light from the fiber in figure 3.2.4a is coupled onto a polarizer followed by a motorized half-waveplate and a polarizing beam splitter before reaching the spectrometer. A legend for all the optical equipment used in this figure can be found in figure 3.2.2a.

When the sample has been mounted in the cryostat, cooled down and the excitation- and extraction paths have been aligned, the localization of good quantum dot candidates can begin. This is done by probing the sample, i.e. moving the sample using the piezo-electric stages it is mounted on, and looking at the spectra it emits when excited with the laser. The setup for characterizing the QDs is shown in figure 3.2.4a and 3.2.4b. The laser is an *APE PicoEmerald 1*, which is a pulsed, tunable laser, ranging from 1080 nm to 1950 nm, with a repetition rate of 80 MHz.

Finding and characterising a dot was by far the most time consuming part of this thesis, as multiple dots were found and had to be characterized to check if they had a bright emission from the X and XX located in the range 1545-1555 nm while also having a low FSS and low background noise. A typical spectra for a quantum dot with a X and XX from this sample is seen in figure 3.2.5. The difference in emission wavelength between the X and XX is ~ 5.5 nm with the X having higher energy. There were also typically one or two peaks close to the X and the XX but also a couple of peaks between them. It is possible to see what peaks belong to a QD as they all increase or decrease when moving around close to the dot.

The Excitation Station

The cryostat used to cool down the sample was a *Montana Instruments, Cryostation s50* and had a working temperature at around 17 K. Located inside the cryostat are the piezo electric stages, consisting of two *Attocube ANPx101* and one *Attocube ANPz101* as well as a microscope objective, *Attocube LT-APO*, with a focal length of 2.89 mm.

There are advantages of having a lower working temperature e.g. lower background noise but there are also advantages of having a higher temperature as the emission is in general brighter. For the sample used in this thesis, a temperature close to 12 K resulted in quite dim QDs while a temperature of 20 K resulting in a lot of background noise and 17 K gave a quite good balance between brightness and noise.

The piezo electrical stage has three degrees of freedom, x , y and z . The resolution is 200 nm with a top range of 5 mm in all directions. When searching for QDs, the first thing to do was to get the sample in focus using the z axis. After the sample was in focus of the objective the probing was done by moving in x/y by $\sim 1\mu\text{m}$ and then moving in y/x tens of μm . This was repeated until a spectra that looked promising was found, see figure 3.2.5, whereupon all the degrees of freedom were optimized one after another, over and over, until the best spectra for the dot was found.

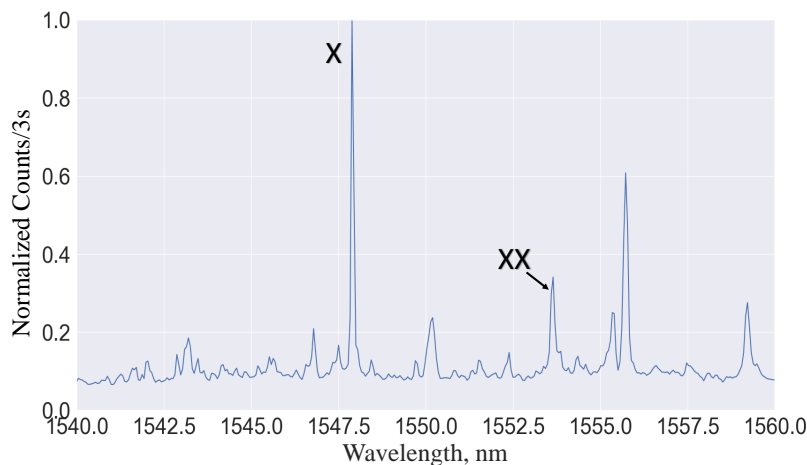


Figure 3.2.5: Example of a good spectra for a QD. The peaks are narrow and quite isolated. In this normalized spectra the X line is located at around 1548 nm and the XX line is located at 1553.5 nm. The lines close to X and XX as well as the line in between all belong to the QD. This is a typical spectra for a QD with an exciton, biexciton pair for this wafer sample.

The spectrometer used was a *Princeton Instruments OMA V* equipped with an InGaAs

array with 1×1024 pixels in the 1000 nm to 1600 nm wavelength range. The pixel to pixel resolution is 0.05 nm for a slitwidth of 25 μm at a wavelength of 1550 nm. As seen in figure 3.2.4b there is a half waveplate that the light passes through before going through a PBS and reaching the spectrometer. This is used to do a polarization sweep of the QD by rotating the waveplate 360° in small increments and recording the spectra for each step. The result from this was used to calculate the FSS by looking at the shift in energy for the X and XX depending on the polarization. This was done by using a script made by previous members of the QNP group.

Additionally, we also did a power sweep measurement of the QD to see how the X and XX behaved for different excitation powers. To do this the laser passes through a half waveplate located in between two polarizers, as seen in figure 3.2.4a, and by rotating the half waveplate the power measured by the powermeter will change. This was also done by changing the excitation power in increments of choice going from a starting power of $\sim 5 \mu\text{W}$ to a power of $\sim 100 \mu\text{W}$, where the X would decrease in brightness.

3.3 Time Correlation Measurements

There were two time correlation measurements made, the g^2 -measurement and the cascade. The g^2 -measurement is used to test the purity of the single photon source. This is to make sure that there is no emission from another transition being excited by the laser. The cascade measurement is made to verify that the X and XX are in fact an entangled, cascaded biexciton-exciton pair. Both of the measurements were done in the lab at KTH and the lab at Ericsson. The cascade measurement was also used to sync two time taggers.

3.3.1 Second Order Correlation Measurements

To test the purity of the single photons from the QD the g^2 -measurement was used. There were QDs that seemed to be bright single photon emitters with an X and a XX with a FSS below $20 \mu\text{eV}$ but then when the g^2 -measurement was done it was clear that the X or the XX were not a pure single photon source. Hence, a QD could be deemed of poor quality even after passing the first characterization. A g^2 -measurement was done for the X and the XX at KTH and a g^2 -measurement was made for the X at Ericsson.

The XX was not bright enough to send to Ericsson as there would only be \sim 100-200 counts detected in Kista and with dark counts close to 100 /s, this would not give any useful results. The losses from KTH to Kista, including the losses of the optical setup in the Ericsson lab, are 91.1 % and with a detection efficiency of 30% the source has to be quite bright.

The setup for the g^2 -measurement at KTH is in figure 3.2.4a combined with figure 3.3.1. The dot is excited in the same way as before and is then sent through a grating that splits up the single photons into different arms depending on the wavelength. Here the X is sent into one arm and the XX is sent into another. For the g^2 -measurement only X or XX was looked at at a time due to the number of detectors at our disposal. The photon of interest, X or XX, was sent through a 50/50 BS and then both of the paths were coupled to the detectors.

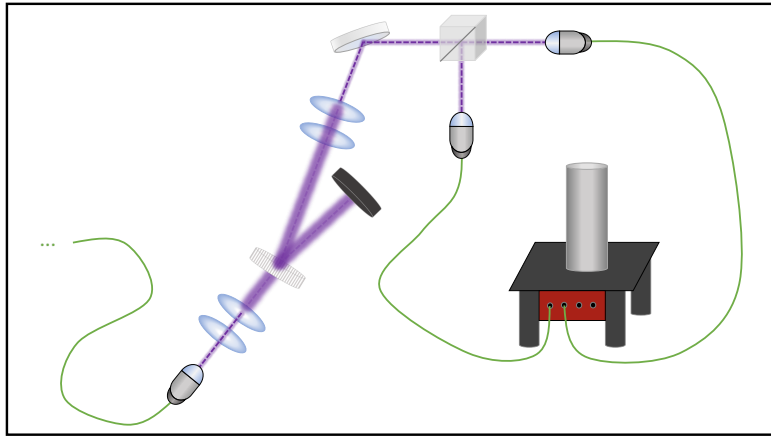


Figure 3.3.1: Optical setup for the g^2 -measurement. The light from the fiber in figure 3.2.4a passes through two lenses, then passes through a grating that spreads out the beam depending on wavelength. The wavelength for the X and XX are coupled in two separate arm that contains two lenses. Either of these arms can be put on a 50/50 BS which outputs are coupled into fibers connected to the SNSPDs. A more in depth description of this setup can be found in [36]. A legend for all the optical equipment used in this figure can be found in figure 3.2.2a.

When doing the g^2 -measurement at Ericsson the setup is essentially the same but given the 18 km fiber between KTH and Ericsson there is a lot of background noise that has to be filtered out. This is done by reflecting the light of a reflective Notch Filter (NF) with 0.7 nm bandwidth, and coupling the desired wavelength, the X in this case. See figure 3.3.2 for the setup at Ericsson. There is also a polarization stabilization setup consisting of 2 two quarter wave-plates and one half-waveplate that can be mounted on the optical table before the light beam is reflected off the NF.

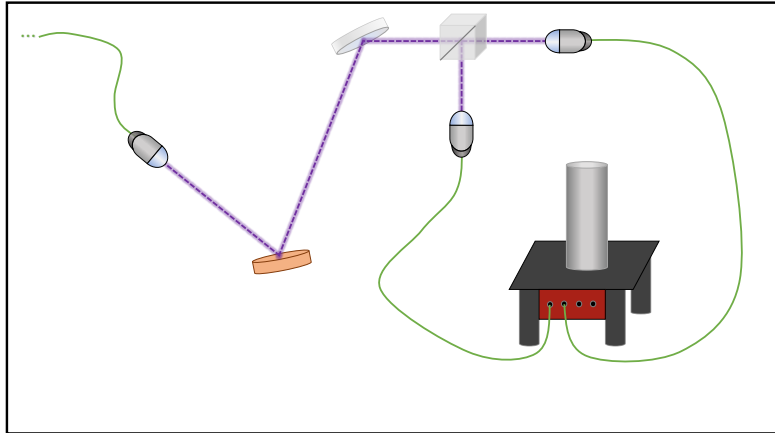


Figure 3.3.2: Optical setup for the g^2 -measurement in Kista. The fiber in figure 3.2.4a is connected to the deployed 18 km long fiber to Kista. The fiber is then coupled onto a NF where only the targeted wavelength of the X is reflected off onto a BS with both outputs coupled to the SNSPDs in Kista. A legend for all the optical equipment used in this figure can be found in figure 3.2.2a.

3.3.2 Cascade Measurements

The setup for the cascade measurement is almost identical to the g^2 -measurement with the only difference being that the BS is no longer at place and instead the X is connected to one detector and the XX is connected to the other one. For a complete setup of the cascade at KTH combine figure 3.2.4a with figure 3.3.3. When doing the cascade cross lab, the X was sent to Ericsson and detected using the SNSPDs there while the XX was detected in the KTH lab. This measurement comes with a new challenge, the data from two different time taggers needs to be synchronized in order use the data from the two time taggers together. To achieve this a post processing synchronization algorithm was created. It was first tested by using two time-taggers for the cascade measurement at KTH to make sure it was possible to do and then it was tested for a cascade measurement where the X was measured in Kista and the XX was measured at KTH. This is done so that the time taggers used in the different labs will agree on the absolute time at which the photons arrive.

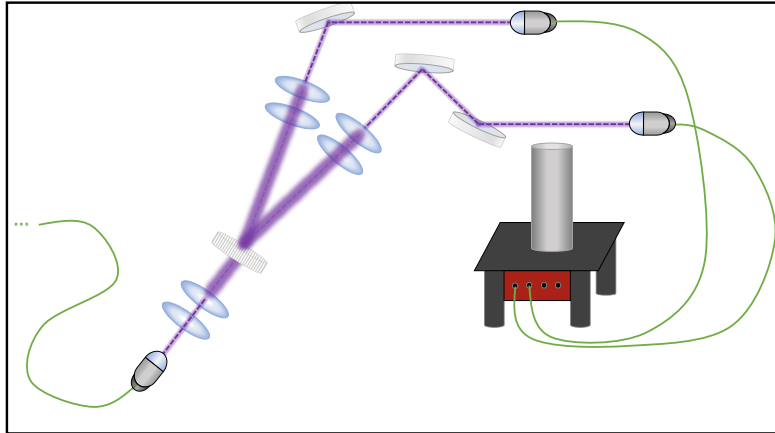


Figure 3.3.3: Optical setup for the cascade measurement. The light from the fiber in figure 3.2.4a passes through two lenses, than passes through a grating that spreads out the beam depending on wavelength. The wavelength for the X and XX are coupled in two separate arm that contains two lenses. Both of these light beams are then coupled into fibers that are connected to the SNSPDs. A more in depth description of this setup can be found in [36]. A legend for all the optical equipment used in this figure can be found in figure 3.2.2a.

Syncing Time-Taggers

In order to compare data from KTH and Ericsson, synchronization of the two time-taggers needs to be realised. Also, if QKD is to be implemented it is important that both parties can agree on which qubits arrived first so their keys are identical. To synchronize two time taggers, the distinct appearance of the cascade plot was used, see figure 3.3.4. The zero peak is substantially higher than the other peaks and thus makes for a good check if the time taggers have been synced. However, since the zero peak only appears when the delay between X and XX is close to the correct value, it is of little use when trying to optimize the delay by looking at the zero peak without a good estimate, as the range can be all from a few ns to several seconds. Although it can be used if one were to do a brute force optimization code, checking 1 ps at a time but it will take a long time to do $\sim 10^{12}$ iterations and also require a lot of allocated memory. Instead the focus was on the wavelike pattern of the other peaks with the repetition rate of 12.5 ns, which stems from the 80 MHz pulse rate of the laser. The algorithm that is used to sync the data uses a Fourier transform and maximized the Fourier amplitude corresponding to 80 MHz frequency by changing the delay between the X and the XX. Also, when using QuTAGs it is important to find the start of the measurement on the QuTAGs internal clock to ensure that the time difference between the two QuTAGs is not in the order of days. To make sure the QuTAGs do not drift in time an external 10

MHz oscillator is connected

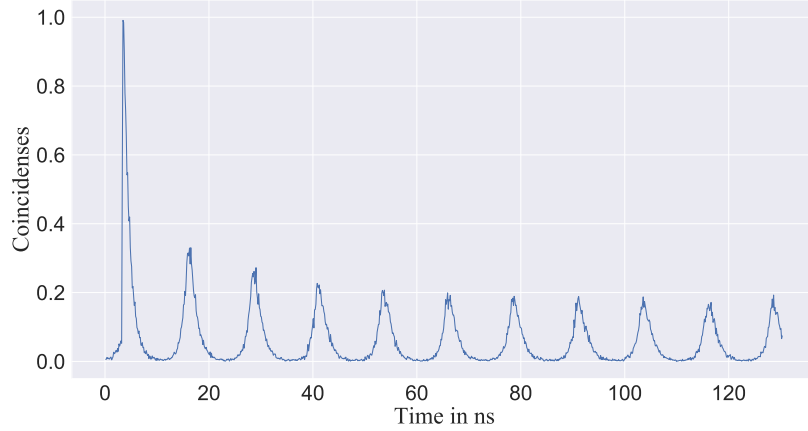


Figure 3.3.4: Typical appearance of the cascade histogram. The high *zero* peak comes from correlating X and XX from the same cascaded decay.

Since there are so small time windows involved with the syncing, it is of great importance that the two time taggers start to record the data as close as possible in time. Only a few seconds of uncertainty when starting the two time-taggers will result in a longer computation time as there are such a large number of integration steps in one second that needs to be checked. Therefore, a script was used when starting the measurements so that only a few ms will be the time difference between the two time taggers.

Chapter 4

Result

In this chapter the results of all the measurements will be presented and discussed. Starting with the characteristics of the QD followed by the g^2 - and cascade-measurements done at KTH and Ericsson.

4.1 The Quantum Dot

4.1.1 Photo-Luminescence Spectra

The photo-luminescence spectra of the QD used in this thesis is presented in figure 4.1.1. The dot is excited into the p-shell using a 80 MHz laser at 1470 nm wavelength with 33 μW of power. The exciton emission can be found at 1548.9 nm wavelength with a peak value of \sim 2400 counts/3s and the biexciton is at 1554.4 nm with \sim 600 counts/3s. The background noise is quite low at \sim 150 counts/3s. The X emission being brighter indicates that there are excitons being excited directly and not all come from a exciton-biexciton decay.

A problem encountered in this thesis was that the Montana cryostat containing the QD was quite unstable, varying in temperature between 10-24 K. This made it so that the QD had to be re-located by using the piezo electrical stages and the brightness of the QD varied a lot with the temperature. The brightest spectra can seen in figure 4.1.1. The cryostat problem has been resolved through refurbishment at the time of writing this thesis and it is now stable at 9 K.

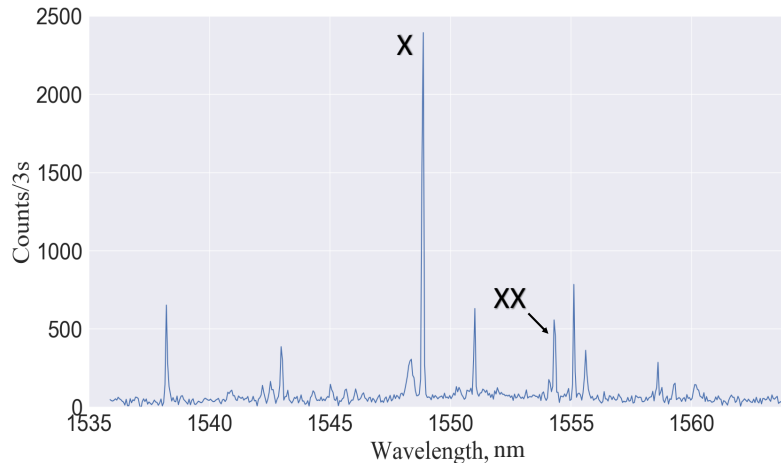


Figure 4.1.1: Shows the emission spectra of the QD when excited with the 80 MHz pulsed laser at wavelength 1470 nm with an excitation power of $33 \mu\text{W}$.

4.1.2 Polarization Series

The polarization series result from section 3.2.2 for the X and XX emission is shown in figures 4.1.2 and 4.1.3 respectively. For a full image of the spectra of the polarization series measurement for the QD see figure A.2.1 and A.2.2 in the appendix. For both the X and XX the emission wavelength is dependent on the rotation of the half wave-plate, hence the emission is polarized. Looking at the shift in wavelength and comparing the emission line of the X with the XX, we can see that they are correlated as they shift in opposite direction at the same time. This is a clear indication that the two lines come from a biexciton-exciton cascade as the energy shift due to the FSS will decrease the wavelength of one decay and increase the wavelength of the other as seen in figure 2.2.3.

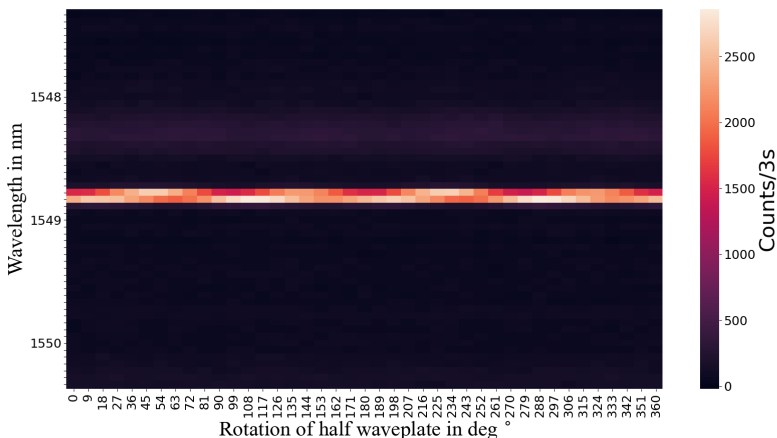


Figure 4.1.2: Shows the emission line from the X during the polarization rotation when excited with the 80 MHz pulsed laser at wavelength 1470 nm with an excitation power of $33 \mu\text{W}$.

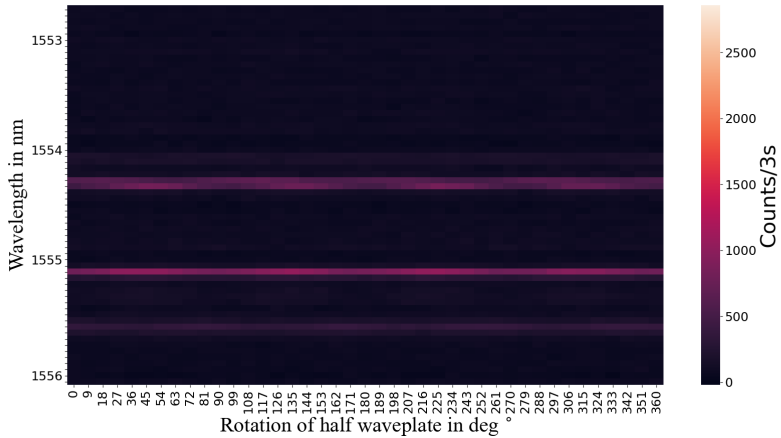


Figure 4.1.3: Shows the emission line from the XX during the polarization rotation when excited with the 80 MHz pulsed laser at wavelength 1470 nm with an excitation power of $33 \mu W$.

By peak-fitting the X and XX in figure 4.1.1 and using the data from the polarization series, the energy fluctuations seen in 4.1.2 and 4.1.3 can be approximated, see appendix A.2.3 for X and A.2.4 for XX. By adding the two energy oscillations together the FSS can be approximated for the biexciton-exciton cascade as twice the amplitude from figure 4.1.4 resulting in $\delta_{FSS} = 7.48 \pm 0.45 \mu eV$. This is a quite low FSS and is still useful for entanglement measurements. However, as discussed in section 2.2.2 the FSS will cause the intermediate X state to evolve in time as seen in equation 2.11. In order to measure this a time resolution higher than $\frac{\hbar}{\delta_{FSS}} \sim 10^{-10} s$ is needed which our SNSPDs are capable of doing [16]. Also as mentioned in section 2.2.2 the two emitted photons from the biexciton-exciton cascade are still maximally entangled given a low FSS [36]. Having a low FSS is also very important in order to guarantee the security of QKD as the two polarization states should not be possible to distinguish based on their wavelength. Hence, a FSS of $0 \mu eV$ would be ideal as the two decay paths of the cascade would emit photons with the same wavelength.

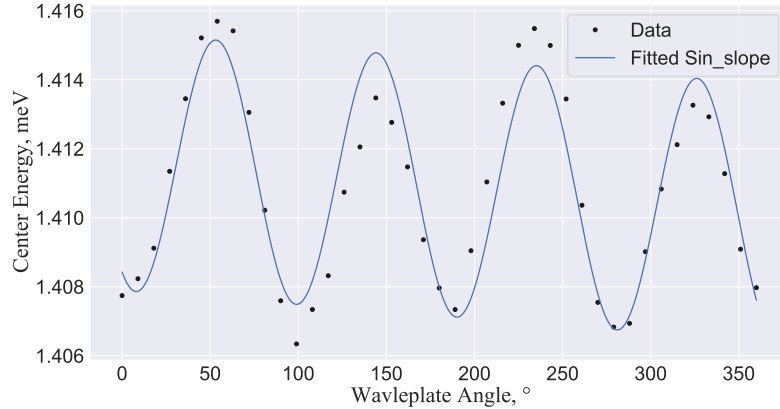


Figure 4.1.4: Shows the average energy oscillation of the photons for different polarization. The FSS corresponds to twice the amplitude of the fitted curve and is $7.48 \pm 0.45 \mu\text{eV}$.

4.1.3 Power Sweep

In figure 4.1.5 the emission spectra is shown for the QD when increasing the excitation power from $\sim 5 \mu\text{W}$ to $\sim 100 \mu\text{W}$ in increments of $5.5 \mu\text{W}$. The X emission gets over-saturated with the increase in power and reaches its peak values at around $30\text{-}40 \mu\text{W}$ while the XX emission is increasing monotonously which can be seen in figure 4.1.6 more easily. This can be understood as for low excitation power, it is more likely to get one X into the QD than two, as there are less excited carriers. With an increase in excitation power, more and more excitons are created resulting in a higher probability of two excitons ending up inside the QD. This results in saturation and eventually a decrease in X emission as the probability of another exciton entering the QD before the X state can decay increases with the excitation power. Furthermore, this is also why the XX emission continues to increase [5]. Hence, there is a trade-off between the X and XX brightness and depending on the measurement, different power levels should be used. It is also worth noting that the background noise also increases monotonously which should be taken into consideration when deciding the excitation power for a measurement.

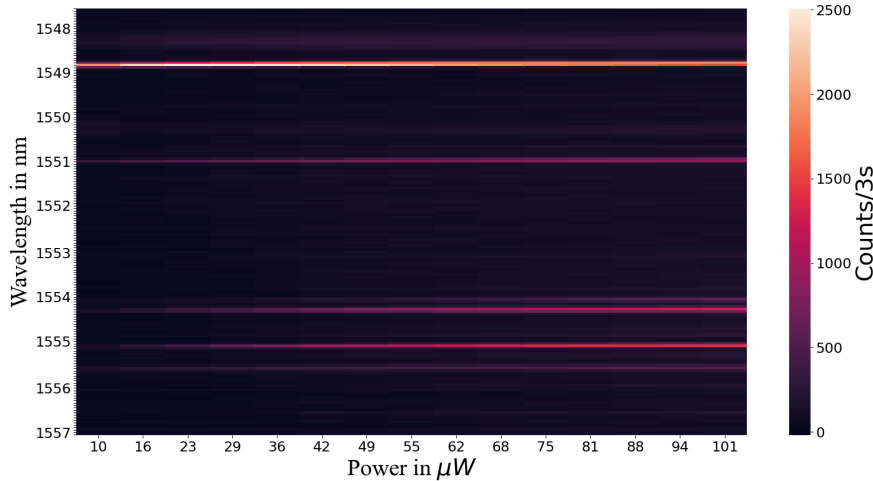


Figure 4.1.5: Shows the emission from the QD from the power sweep measurement, starting at $\sim 5 \mu\text{W}$ going to $\sim 100 \mu\text{W}$.

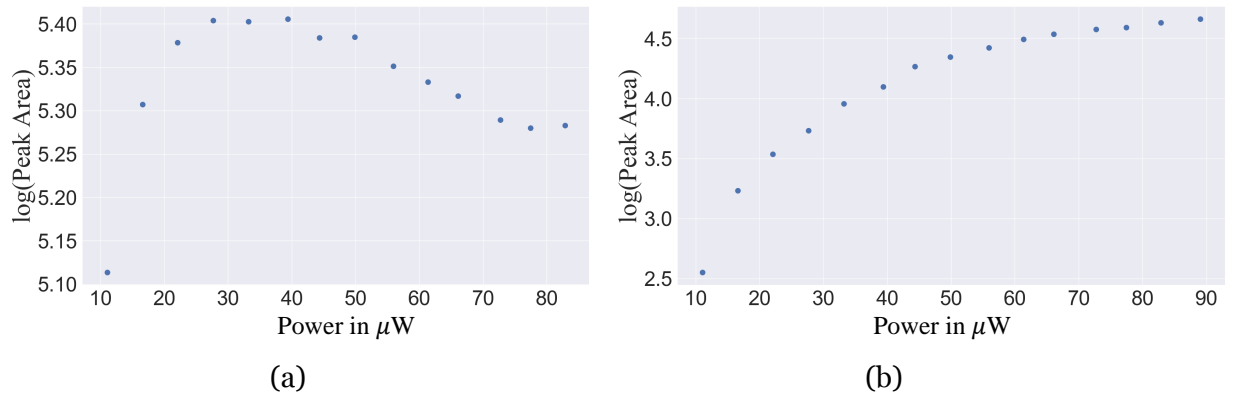


Figure 4.1.6: **a)** Power dependence for the X. **b)** Power dependence for the XX. Both of these figures were created by curve fitting the spectral line of the X/XX and integrating the area of the peak at each power level.

4.2 G2-Measurement

Figure 4.2.1 and 4.2.2 shows the g^2 -measurements done in the KTH lab for the X and XX respectively. The dip in the middle of the histogram shows that the photons are anti bunching and corresponds to the true zero in time as the time axis indicates the delay between detection events on the two channels. Hence, there are almost no simultaneous detection events in these plots, and both photons come from a single photon emitter. The g^2 -value was calculated by dividing the integrated area of the zero peak with the average of the side peaks areas. The error is approximated as $\Delta g^2(0) = g^2(0) \sqrt{\left(\frac{1}{x_1} + \frac{1}{x_2}\right)}$ where x_1 is the area of the zero peak and x_2 is the average area of the side peaks. By looking at Figures 4.2.1 and 4.2.2, it is clear that the $g^2(0)$

value is much lower for the X at $g^2(0) = 0.049 \pm 0.003$ compared to the XX with $g^2(0) = 0.169 \pm 0.020$. This is due to the emission from the X being brighter than the XX. Also, from figure 4.1.1 it can be seen that the X is well isolated, making possible to filter out any bright peaks close by. While the XX has a small peak close by that is seemingly possible to filter out, it could still be slightly overlapping with the XX peak and thereby diluting the purity of the XX emission. The distance between the peaks is 12.5 ns due to the 80 MHz repetition rate of the laser, as the QD can be excited by every pulse. The lifetime of the X state was measured to 1.23 ns long (the XX state is typically shorter [36]), see figure A.2.6 in the appendix. It should also be mentioned that the number of counts on the SNSPDs are much higher than on the spectrometer. On the SNSPD the X emission is $\sim 14\,000 \pm 3000$ counts/s and $\sim 4000 \pm 1500$ counts/s for the XX, which is expected as the SSPD are much more sensitive than the spectrometer as it can detect a single photons. The count rate from the spectrometer plot is also not accurate as one needs to integrate the peak to get the photon numbers, as done in 4.1.4.

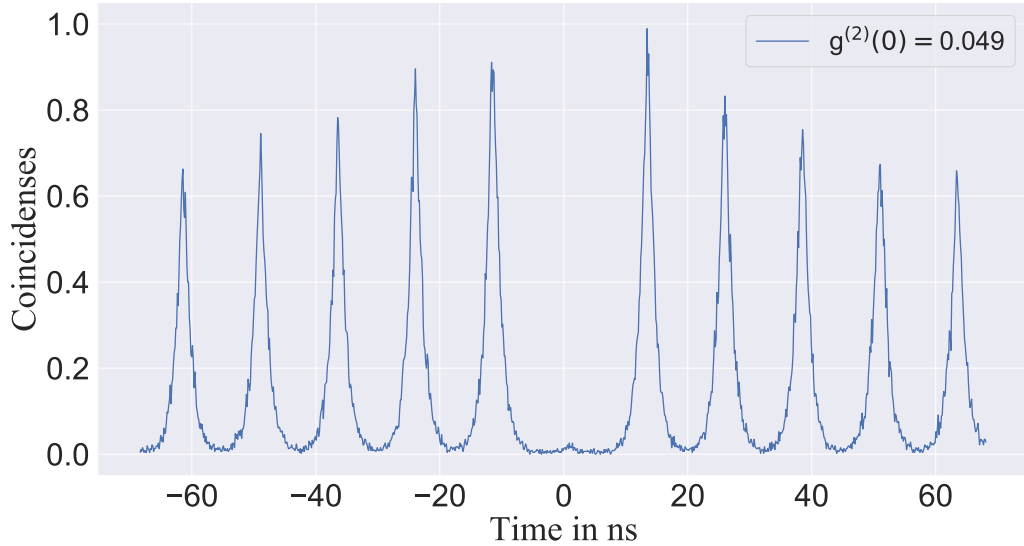


Figure 4.2.1: g^2 -measurement for the X emission at KTH. The value for the second order coherence at no delay is $g^2(0) = 0.049 \pm 0.0026$. The data was recorded for ~ 20 minutes with a average count rate of $\sim 14\,000$ counts/s on both channels. The bin-size used in this plot was 128 ps.

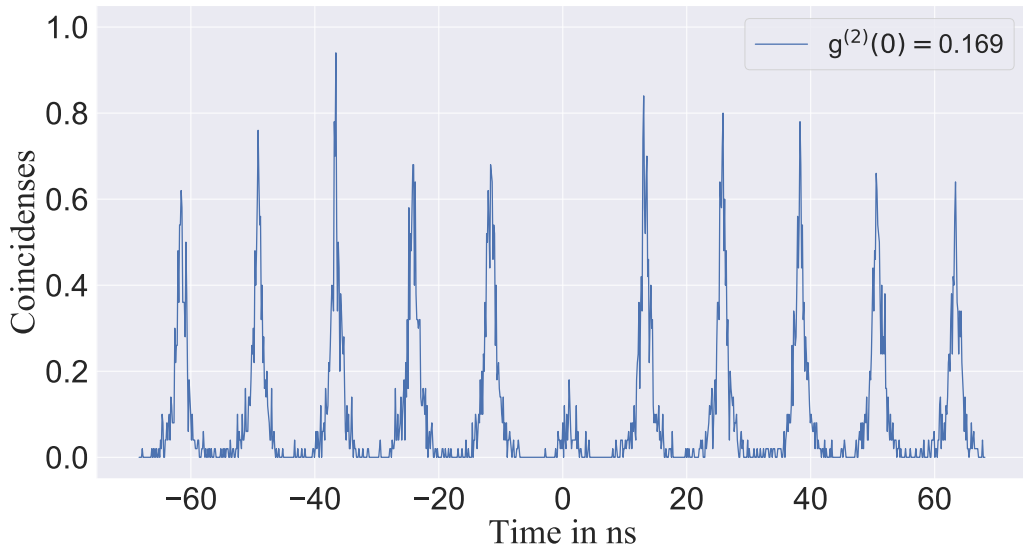


Figure 4.2.2: g^2 -measurement for the XX emission at KTH. The value for the second order coherence at no delay is $g^2(0) = 0.169 \pm 0.020$ with a average count rate of ~ 2500 counts/s on both channels. The data was recorded for ~ 80 minutes. The bin-size used in this plot was 128 ps.

Figure 4.2.3 shows the g^2 -measurement for the X recorded at Ericsson in Kista. The high losses, 91.1%, as well as background noise from the 18 km fiber increased the value significantly to $g^2(0) = 0.176 \pm 0.0191$. This is still a good g^2 -value as it is clear that the photons come from a single photon source ($g^2(0) < 0.5$ qualifies a single photons source as $g^2(0) = 1 - \frac{1}{n}$ applies for Fock states). This is also a good result as it shows that a small g^2 -value in the lab is necessary if the source is going to be used in out of lab implementations such as QKD given the current infrastructure with high losses and background noise. Due to the high losses to Kista only the X was measured at Ericsson as the XX was too dim. When deciding the excitation power for the g^2 -measurement at Ericsson it was done with the goal of having the X emission as bright as possible. The photon count rate at Ericsson for this measurement was on average 2000 counts/s for the X.

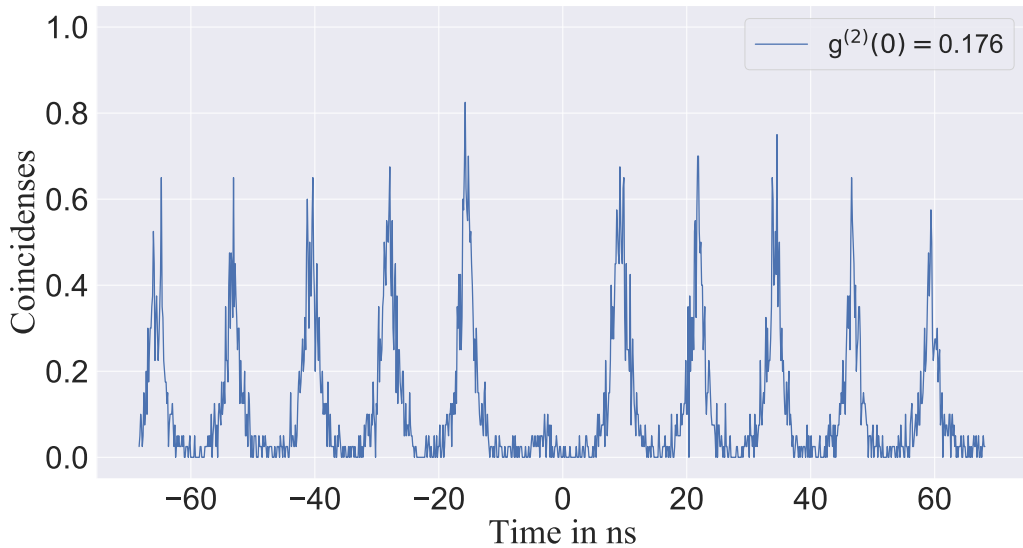


Figure 4.2.3: g^2 -measurement for the X emission at Ericsson. The value for the second order coherence at no delay is $g^2(0) = 0.176 \pm 0.0191$. The data was recorded for ~ 20 minutes with a average count rate of ~ 1000 counts/s on both channels. The bin-size used in this plot was 128 ps.

4.3 Cascade Measurement

In figure 4.3.1 the cascade histogram is shown with the data recorded using two different time-taggers. The time-taggers were connected to one output channel each from the detectors while also being connected to one and the same 10 MHz external oscillator. The distinct cascade appearance is visible and it is clear that the two spectral lines in figure 4.1.1 indeed are a XX-X pair. The cascade histogram is generated by looking at the time difference between XX photons and X photons. The first peak is higher as it corresponds to the time difference between the XX photon and the X photon from the same biexciton-exciton cascade. This is also why the peak is asymmetric, as only the X state lifetime is recorded in this peak, seen as the falling slope. While for the other peaks, cross-correlating X and XX photons from different biexciton-exciton cascades, the lifetime of the XX state can be seen as the rising slope resulting in a more symmetric peak. The synchronization time to find the offset between the two time-taggers data files took ~ 25 min, this excludes the possibility of doing real time synchronization. However, after the time delay has been found once, it should be possible to do it much faster given the time delay from the first synchronization.

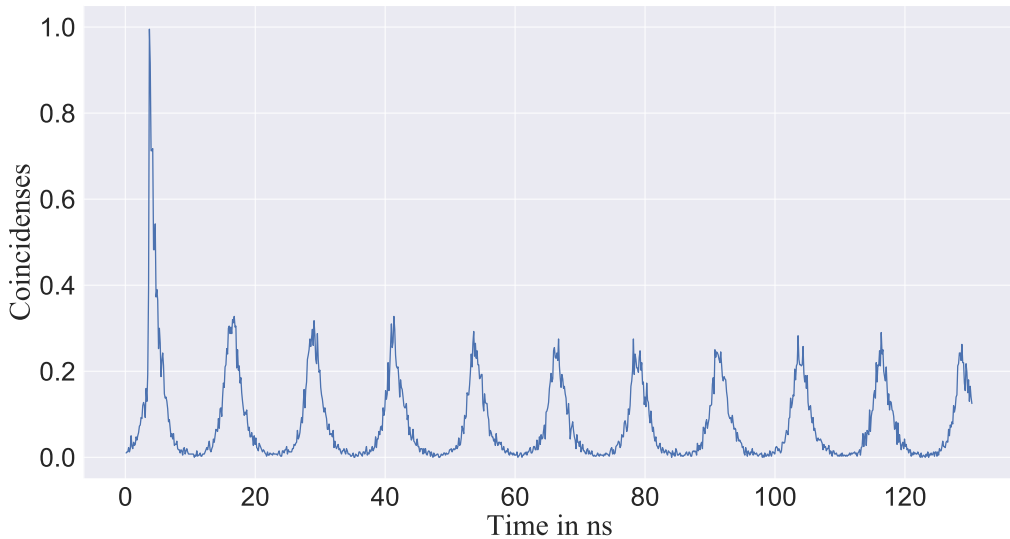


Figure 4.3.1: Shows the cascade histogram for two synchronized time-taggers. The data was recorded for ~ 20 min with a average count rate of 14 000 counts/s for the X and 9 000 counts/s for the XX. The bin-size used in this plot was 128 ps.

A comparison between the synchronized cascade histogram generated from two time-taggers and the cascade histogram generated by using one time-tagger is shown in figure 4.3.2. The synchronized cascade is not as clean looking as the histogram of the single time-tagger, with a lower ratio between the zero peak and the subsequent peaks. This is most likely due to the count rate for the two time-tagger measurement being lower than the single QuTAG measurement as the coupling of the X and XX emission drifted away due to change in temperature in the cryostat, causing the count rate to decrease during the measurement. The count rate for the single time-taggers cascade measurement was stable at around 22 000 counts/s for the X and 18 000 counts/s for the XX. While for the two time-tagger cascade the count rate dropped linearly from 18 000 counts/s to 12 000 counts/s for the X and from 12 000 counts/s to 6000 counts/s for the XX. To facilitate the difference between the two histograms both have been normalized. Overall, the synchronized histogram is very similar to the histogram generated using one QuTAG, especially given the problems encountered during the measurement.

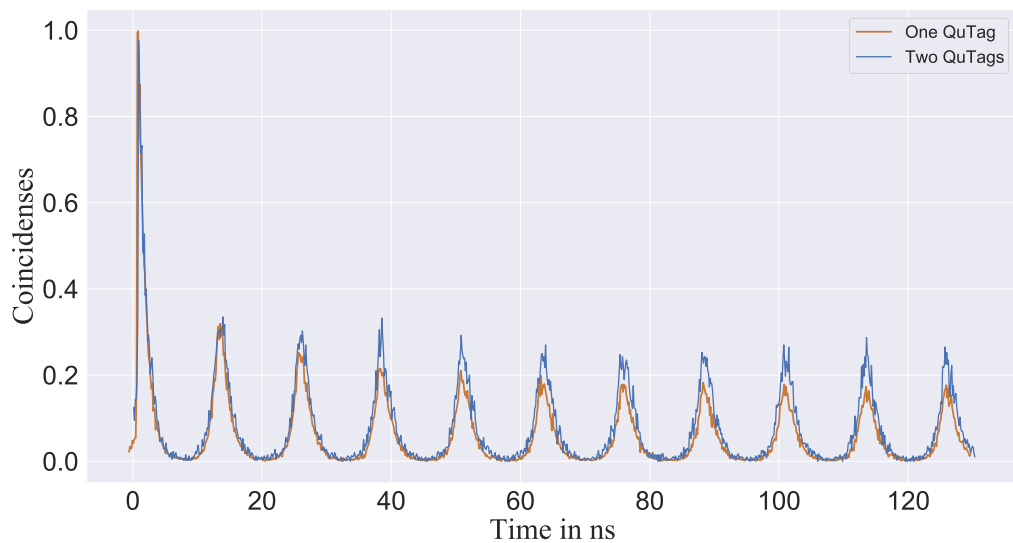


Figure 4.3.2: Comparison between the cascade measurement done when using two qutags and one QuTAG. Bin-size used was 128 ps for both histograms.

Chapter 5

Conclusion

In this thesis we have investigated and tested the setup needed to share quantum information across a metropolitan network based on single photon communication. First, we characterised the new set of SNSPDs at KTH. Second, we installed the SNSPDs at the Ericsson lab, thus completing the quantum link of about 18 km. Third, the single photon light source, based on QDs, was characterised and used to send quits over a deployed fiber to generate a $g^2(0)$ -value of 0.17. Finally, we used the XX-X cascade from the QD to perform time synchronisation of two time-taggers.

Quantum Dot

Overall the quantum dot used in this thesis preformed well and would be usable in some photonic applications, albeit a little dim, it still produced over 20 000 counts/s with a 80 MHz excitation frequency. There are some improvements that can be done in future work when it comes to the QD. As mentioned in the previous chapter, a problem encountered when working with the QD was that the cryostat was unstable and varied a lot in temperature, from 10-24 K. This has been fixed and should not be a problem in the future. Nevertheless, it would be of great benefit if there was an easier way to located the QDs in the sample as currently they are located randomly inside the sample without any grid to help orientate.

When it comes to increasing the brightness of the QD there are a few ways to achieve this. The use of a Solid Immersion Lens (SIL) could be used to increase the extraction rate, as used in [32] for dots in the telecom O-band, when a good candidate has been identified. However, the current statistical nature in creating the QDs makes this into

a guessing game as either the SIL would be mounted on the sample before probing for QDs and then hope that there is at least one good QD inside the area of the SIL. Or a good QD has to be found and the SIL can then be mounted on top of the dot. This brings us back to the re-location problem where a systematic way of finding a specific dot would be of great value. Another option for increasing the brightness could be to grow the QDs in parabolic micro cavities as used in [17] to increase the photon extraction rate from the dots.

Lastly, another aspect that should be considered is the FSS. Currently the odds of finding a good QD with a XX-X cascade that gives low g^2 -values for both emissions as well as having a low FSS are low. If the sample could be strain tuned to adjust the FSS the odds of finding a QD that is usable would increase. This has been done in [16] where a reduction of $5 \mu\text{eV}$ in FSS was achieved.

Correlation Measurements

The g^2 -value measured for the X at KTH was very low at 0.049 which proved to be useful when sending the X photons over the 18 km of deployed fiber to Kista. The XX on the other hand could benefit from having a cleaner excitation to reduce any dilution in the g^2 -measurement and also increase its brightness. This could be done by using two-photon resonant excitation as used in [35]. However, the fact that the g^2 -value measured for the X at Ericsson is comparable to the XX's value in lab is an acceptable result as both g^2 -values were far below the single emitter limit of 0.5.

From the cascade measurement it is clear that the X and XX photons can be used to synchronize two time-taggers and has been suggested in [1] and [6]. However, the synchronization between the QuTAG in Kista and the one at KTH has not yet been accomplished and is the next logical step looking forward. Currently the synchronization only worked with the two time-taggers at KTH when connected to the same 10 MHz oscillator. For the cascade measurement over the 18 km of deployed fiber between Kista and KTH, the external oscillators differ. The one at KTH is a very precise rubidium source while the one in Kista is a high end Vector Network Analyzer (VNA). This could contribute to difficulties in synchronization if the relative time between the two QuTAGs varies in time. Installing a rubidium source in Kista would make it possible to reduce the spread in uncertainty. Also, the synchronization algorithm could benefit of having some extra features added. The idea of optimizing

the 80 MHz Fourier amplitude is working effectively to find a rough estimate but a peak finding function for the zero peak has yet to be implemented. Adding this as well as a peak optimization function for the zero peak height would allow for a more automated synchronization and allow for larger time spans to be tested.

Outlook

To achieve QKD between KTH and Kista there are still some challenges left to solve. Firstly the synchronization between the time-taggers in KTH and Kista must be addressed. As stated in the previous paragraph, the synchronization code would benefit from having some more work done and using a rubidium source for the 10 MHz oscillator in Kista would hopefully help as well. Other than this the polarization stabilization, see [4], would have to be added to the optical setup. Also implementing a code to run the E91 protocol is left to be done. As a final note on this topic, like mentioned earlier, the current synchronization algorithm is far from real time synchronization when done at first, yet if a synchronization between the two time-taggers has been established it is expected to take considerably less computation time, in the order of seconds, to synchronize once more.

The current setup can be used for other single photon applications than QKD. The generation and distribution of randomness is something that has been discussed within the QNP group and is being looked into. The main idea is to guarantee true randomness by exploiting the statistics inherited in a quantum system. The purity of the single photons is tested with a g^2 -measurement where the photons pass through a 50/50 BS. The data recorded can be used to verify the quantum mechanical nature of the photon source given a low g^2 -value (close to zero) and also to generate random bits depending on the beam path taken by the photons. How the random numbers are generated from the data is not trivial as the BS may be biased and hence the distribution will differ from 50/50 causing the need for de-biasing the data.

Bibliography

- [1] Agnesi, Costantino, Avesani, Marco, Calderaro, Luca, Stanco, Andrea, Foletto, Giulio, Zahidy, Mujtaba, Scriminich, Alessia, Vedovato, Francesco, Vallone, Giuseppe, and Villoresi, Paolo. “Simple Quantum Key Distribution with qubit-based synchronization and a self-compensating polarization encoder”. In: (Sept. 2019). DOI: 10.1364/OPTICA.381013. URL: <https://www.osapublishing.org/optica/fulltext.cfm?uri=optica-7-4-284&id=429620>.
- [2] Basset, Francesco Basso, Valeri, Mauro, Roccia, Emanuele, Muredda, Valerio, Poderini, Davide, Neuwirth, Julia, Spagnolo, Nicolò, Rota, Michele B, Carvacho, Gonzalo, Sciarrino, Fabio, and Trotta, Rinaldo. *Quantum key distribution with entangled photons generated on demand by a quantum dot*. 2021, p. 6379. DOI: 10.1126/sciadv.abe6379.
- [3] Bennett, Charles H., Brassard, Gilles, and Mermin, N. David. “Quantum cryptography without Bell’s theorem”. In: *Phys. Rev. Lett.* 68 (5 Feb. 1992), pp. 557–559. DOI: 10.1103/PhysRevLett.68.557. URL: <https://link.aps.org/doi/10.1103/PhysRevLett.68.557>.
- [4] Bensoussan, Sandra. *Polarization stabilization in a deployed fiber for quantum key distribution*. Internal Ericsson Report.
- [5] Brunner, K., Abstreiter, G., Böhm, G., Tränkle, G., and Weimann, G. “Sharp-Line Photoluminescence and Two-Photon Absorption of Zero-Dimensional Biexcitons in a GaAs/AlGaAs Structure”. In: *Phys. Rev. Lett.* 73 (8 Aug. 1994), pp. 1138–1141. DOI: 10.1103/PhysRevLett.73.1138. URL: <https://link.aps.org/doi/10.1103/PhysRevLett.73.1138>.
- [6] Calderaro, Luca, Stanco, Andrea, Agnesi, Costantino, Avesani, Marco, Dequal, Daniele, Villoresi, Paolo, and Vallone, Giuseppe. “Fast and simple qubit-based synchronization for quantum key distribution”. In: (Sept. 2019). DOI: 10.1103/

BIBLIOGRAPHY

- PhysRevApplied. 13 . 054041. URL: <http://arxiv.org/abs/1909.12050> %
20<https://dx.doi.org/10.1103/PhysRevApplied.13.054041>.
- [7] Coles, Berta, Tomamichel, and Wehner. “Entropic Uncertainty Relations and their Applications”. In: *Rev. Mod. Phys.* 89.015002 (2017). DOI: 10.1103/RevModPhys.89.015002. URL: <https://arxiv.org/abs/1511.04857>.
- [8] Duan, L-m, Lukin, M D, Cirac, J I, and Zoller, P. *Long-distance quantum communication with atomic ensembles and linear optics*. 2001. URL: <https://www.nature.com/articles/35106500>.
- [9] Dynes, J. F., Wonfor, A., Tam, W. W.S., Sharpe, A. W., Takahashi, R., Lucamarini, M., Plews, A., Yuan, Z. L., Dixon, A. R., Cho, J., Tanizawa, Y., Elbers, J. P., Greißer, H., White, I. H., Penty, R. V., and Shields, A. J. “Cambridge quantum network”. In: *npj Quantum Information* 5 (1 Dec. 2019). ISSN: 20566387. DOI: 10.1038/s41534-019-0221-4.
- [10] Einstein, A., Podolsky, B., and Rosen, N. “Can Quantum-Mechanical Description of Physical Reality Be Considered Complete?” In: *Phys. Rev.* 47 (10 May 1935), pp. 777–780. DOI: 10.1103/PhysRev.47.777. URL: <https://link.aps.org/doi/10.1103/PhysRev.47.777>.
- [11] Ekert, Artur K. “Quantum cryptography based on Bell’s theorem”. In: *Phys. Rev. Lett.* 67 (6 Aug. 1991), pp. 661–663. DOI: 10.1103/PhysRevLett.67.661. URL: <https://link.aps.org/doi/10.1103/PhysRevLett.67.661>.
- [12] Fox, Mark. *Optical Properties of Solids*. Oxford University Press, 2010.
- [13] Fox, Mark. *Quantum Optics*. Oxford University Press, 2014.
- [14] Infiniquant. *TUTORIAL: CONTINUOUS-VARIABLE QUANTUM COMMUNICATION*. URL: <http://infiniquant.com/tutorial-continuous-variable-quantum-communication/> (visited on 01/28/2021).
- [15] Jia, Huang et al. “High speed superconducting nanowire single-photon detector with nine interleaved nanowires”. In: (2018). URL: <https://iopscience.iop.org/article/10.1088/1361-6668/aac180/meta>.
- [16] Lettner, Thomas, Gyger, Samuel, Zeuner, Katharina D., Schweickert, Lucas, Steinhauer, Stephan, Hedlund, Carl Reuterskiöld, Stroj, Sandra, Rastelli, Armando, Hammar, Mattias, Trotta, Rinaldo, Jöns, Klaus D., and Zwiller, Val. “Strain-Controlled Quantum Dot Fine Structure for Entangled Photon

- Generation at 1550 nm". In: *Nano Letters* (Dec. 2021), acs.nanolett.1c04024. ISSN: 1530-6984. DOI: 10.1021/acs.nanolett.1c04024. URL: <https://pubs.acs.org/doi/10.1021/acs.nanolett.1c04024>.
- [17] Lettner, Thomas, Zeuner, Katharina D., Schöll, Eva, Huang, Huiying, Scharmer, Selim, Silva, Saimon Filipe Covre Da, Gyger, Samuel, Schweickert, Lucas, Rastelli, Armando, Jöns, Klaus D., and Zwiller, Val. "GaAs Quantum Dot in a Parabolic Microcavity Tuned to 87Rb D1". In: *ACS Photonics* 7 (1 Jan. 2020), pp. 29–35. ISSN: 23304022. DOI: 10.1021/acspophotonics.9b01243.
- [18] Lettner, Thomas. *Bright and strain-tunable semiconductor quantum dot devices*. 2021. ISBN: 9789180400725. URL: <http://urn.kb.se/resolve?urn=urn:nbn:se:kth:diva-304685>.
- [19] Lin, Z, Gyger, S, Jöns, K D, and Zwiller, V. *Efficient and Versatile Toolbox for Analysis of Time-Tagged Measurements*. URL: <https://timetag.github.io/>.
- [20] Michler, Peter. *Single Semiconductor Quantum Qots*. Berlin ; New York : Springer Verlag, 2009. DOI: <https://doi.org/10.1007/978-3-540-87446-1>.
- [21] Natarajan, Chandra M., Tanner, Michael G., and Hadfield, Robert H. *Superconducting nanowire single-photon detectors: Physics and applications*. June 2012. DOI: 10.1088/0953-2048/25/6/063001.
- [22] Nuñez, Labato Carlos. *Optimization of MOVPE-grown Quantum Dots for long distance quantum communication* KTH Royal Institute of Technology School of Engineering Sciences. URL: <http://urn.kb.se/resolve?urn=urn:nbn:se:kth:diva-258829>.
- [23] Reddy, Dileep V., Nerem, Robert R., Nam, Sae Woo, Mirin, Richard P., and Verma, Varun B. "Superconducting nanowire single-photon detectors with 98% system detection efficiency at 1550 nm". In: *Optica* 7.12 (Dec. 2020), pp. 1649–1653. DOI: 10.1364/OPTICA.400751. URL: <http://www.osapublishing.org/optica/abstract.cfm?URI=optica-7-12-1649>.
- [24] Schimpf, Christian, Reindl, Marcus, Huber, Daniel, Lehner, Barbara, Silva, Saimon F. Covre Da, Manna, Santanu, Vyvlecka, Michal, Walther, Philip, and Rastelli, Armando. "Quantum cryptography with highly entangled photons from semiconductor quantum dots". In: (July 2020). URL: <http://arxiv.org/abs/2007.12726>.

BIBLIOGRAPHY

- [25] Schweickert, Lucas., Zwiller, Val., Jöns, Klaus D., Warburton, Richard J., and (SCI), KTH Skolan för teknikvetenskap. *Correlation spectroscopy with epitaxial quantum dots Single-photons alone in the dark*. ISBN: 9789178735549. URL: <http://urn.kb.se/resolve?urn=urn:nbn:se:kth:diva-273213>.
- [26] Shor, Peter W. *Polynomial-Time Algorithms for Prime Factorization and Discrete Logarithms on a Quantum Computer* *, pp. 124–134.
- [27] Staffas, Theodor. *Live 3D imaging quantum LiDAR*. URL: <http://urn.kb.se/resolve?urn=urn:nbn:se:kth:diva-297865>.
- [28] Testardi, L. R. “Destruction of Superconductivity by Laser Light”. In: *Phys. Rev. B* 4 (7 Oct. 1971), pp. 2189–2196. DOI: 10.1103/PhysRevB.4.2189. URL: <https://link.aps.org/doi/10.1103/PhysRevB.4.2189>.
- [29] Ursin, R., Tiefenbacher, F., Schmitt-Manderbach, T., Weier, H., Scheidl, T., Lindenthal, M., Blauensteiner, B., Jennewein, T., Perdigues, J., Trojek, P., Ömer, B., Fürst, M., Meyenburg, M., Rarity, J., Sodnik, Z., Barbieri, C., Weinfurter, H., and Zeilinger, A. “Entanglement-based quantum communication over 144km”. In: *Nature Physics* 3 (7 July 2007), pp. 481–486. ISSN: 17452481. DOI: 10.1038/nphys629.
- [30] Wootters·, W K and Zurek, W H. 26. *Van Arsdell*. 1982.
- [31] Xiang, Zi Heng, Huwer, Jan, Skiba-Szymanska, Joanna, Stevenson, R. Mark, Ellis, David J.P., Farrer, Ian, Ward, Martin B., Ritchie, David A., and Shields, Andrew J. “A tuneable telecom wavelength entangled light emitting diode deployed in an installed fibre network”. In: *Communications Physics* 3 (1 Dec. 2020). ISSN: 23993650. DOI: 10.1038/s42005-020-0390-7.
- [32] Yang, Jingzhong, Nawrath, Cornelius, Keil, Robert, Joos, Raphael, Zhang, Xi, Höfer, Bianca, Chen, Yan, Zopf, Michael, Jetter, Michael, Portalupi, Simone Luca, Ding, Fei, Michler, Peter, and Schmidt, Oliver G. “Quantum dot-based broadband optical antenna for efficient extraction of single photons in the telecom O-band”. In: *Optics Express* 28 (13 June 2020), p. 19457. ISSN: 1094-4087. DOI: 10.1364/oe.395367.

BIBLIOGRAPHY

- [33] Yang, Joel K. W., Kerman, Andrew J., Dauler, Eric A., Anant, Vikas, Rosfjord, Kristine M., and Berggren, Karl K. “Modeling the Electrical and Thermal Response of Superconducting Nanowire Single-Photon Detectors”. In: *IEEE Transactions on Applied Superconductivity* 17.2 (2007), pp. 581–585. DOI: 10.1109/TASC.2007.898660.
- [34] Zadeh, Iman Esmaeil, Los, Johannes W.N., Gourgues, Ronan B.M., Chang, Jin, Elshaari, Ali W., Zichi, Julien Romain, Staaden, Yuri J. Van, Swens, Jeroen P.E., Kalhor, Nima, Guardiani, Antonio, Meng, Yun, Zou, Kai, Dobrovolskiy, Sergiy, Fognini, Andreas W., Schaart, Dennis R., Dalacu, Dan, Poole, Philip J., Reimer, Michael E., Hu, Xiaolong, Pereira, Silvania F., Zwiller, Val, and Dorenbos, Sander N. “Efficient Single-Photon Detection with 7.7 ps Time Resolution for Photon-Correlation Measurements”. In: *ACS Photonics* 7 (7 July 2020), pp. 1780–1787. ISSN: 23304022. DOI: 10.1021/acsphotonics.0c00433.
- [35] Zeuner, Katharina D., Jöns, Klaus D., Schweickert, Lucas, Hedlund, Carl Reuterskiöld, Lobato, Carlos Nuñez, Lettner, Thomas, Wang, Kai, Gyger, Samuel, Schöll, Eva, Steinhauer, Stephan, Hammar, Mattias, and Zwiller, Val. “On-demand generation of entangled photon pairs in the telecom C-band for fiber-based quantum networks”. In: (Dec. 2019). URL: <http://arxiv.org/abs/1912.04782>.
- [36] Zeuner, Katharina. *Semiconductor Quantum Optics at Telecom Wavelengths*. ISBN: 9789178736898. URL: <http://urn.kb.se/resolve?urn=urn:nbn:se:kth:diva-285782>.

Appendix - Contents

A Additional Plots	53
A.1 DBR Characterization for the rest of the wafer	53
A.2 Quantum Dot Characterization	60
A.2.1 Polarization Series and FSS	60
A.2.2 Power series	61
A.2.3 Lifetime of the Exciton	62
B ETA Graphs and Code	63
B.1 State Diagrams and ETA Code	63
B.1.1 How to read in a data file in ETA	63
B.1.2 How the g^2 histogram is created using ETA	64
B.1.3 How the cascade histogram is created using ETA	65
B.2 ETA Synchronization Code	65

Appendix A

Additional Plots

A.1 DBR Characterization for the rest of the wafer

In this section the DBR characterization done in subsection 3.2.1 is shown for the remaining areas of the wafer sample seen in figure 3.2.1, as well as the spectra reflected of the mirror.

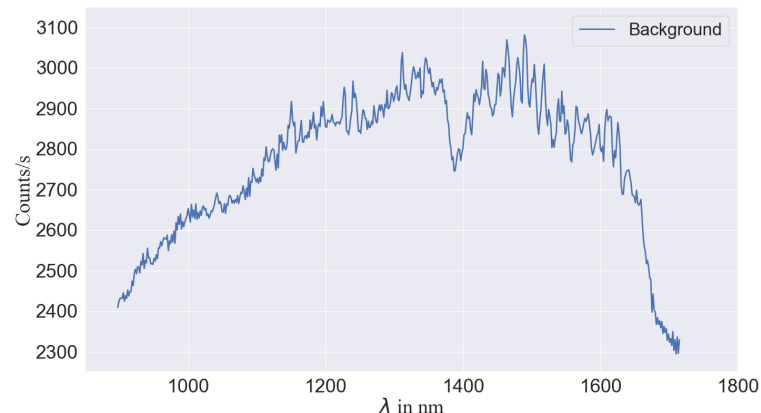


Figure A.1.1: Shows the spectra of the Halogen Light Source HL-200 reflected of the mirror. See figure 3.2.2b for the setup.

APPENDIX A. ADDITIONAL PLOTS

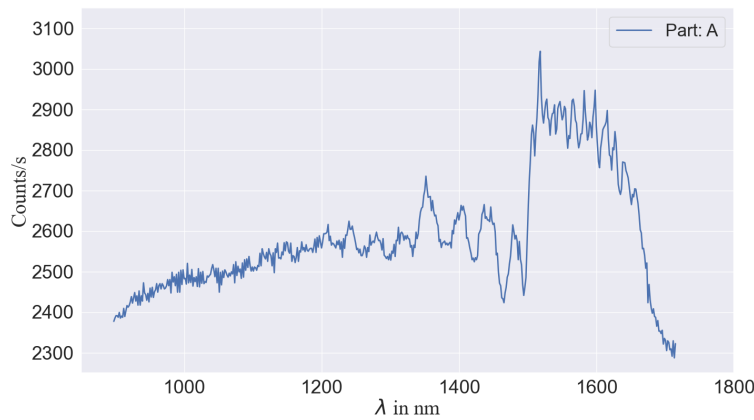


Figure A.1.2: Shows the reflected spectra from part A of sample 8366. See figure 3.2.2b for the setup.

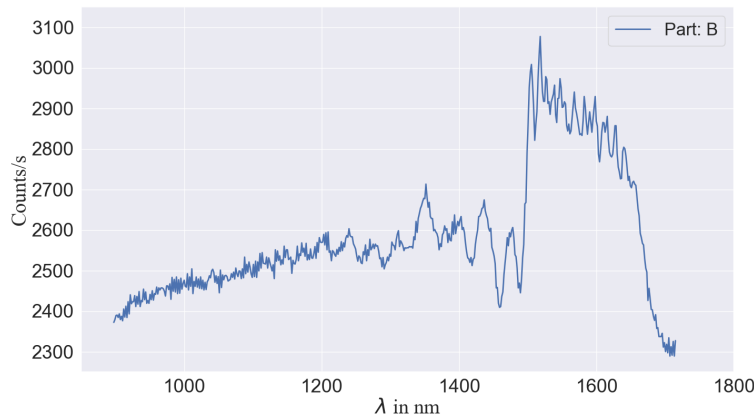


Figure A.1.3: Shows the reflected spectra from part B of sample 8366. See figure 3.2.2b for the setup.

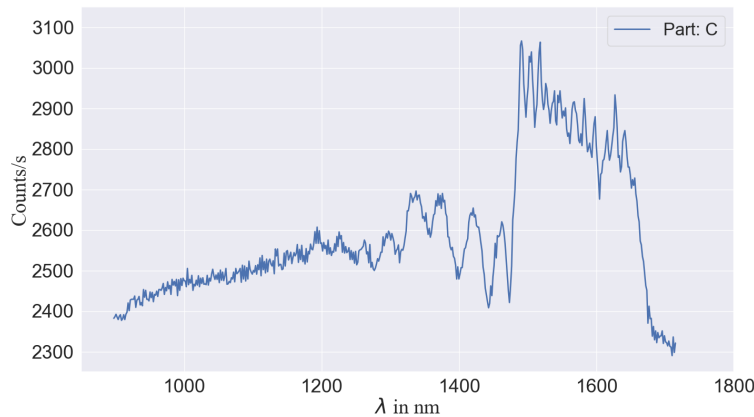


Figure A.1.4: Shows the reflected spectra from part C of sample 8366. See figure 3.2.2b for the setup.

APPENDIX A. ADDITIONAL PLOTS

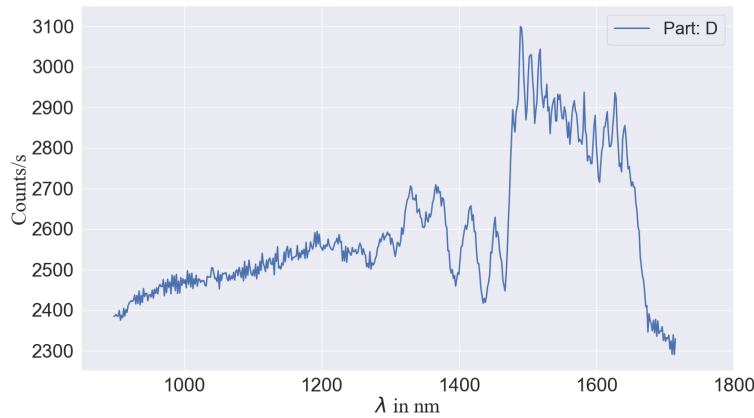


Figure A.1.5: Shows the reflected spectra from part D of sample 8366. See figure 3.2.2b for the setup.

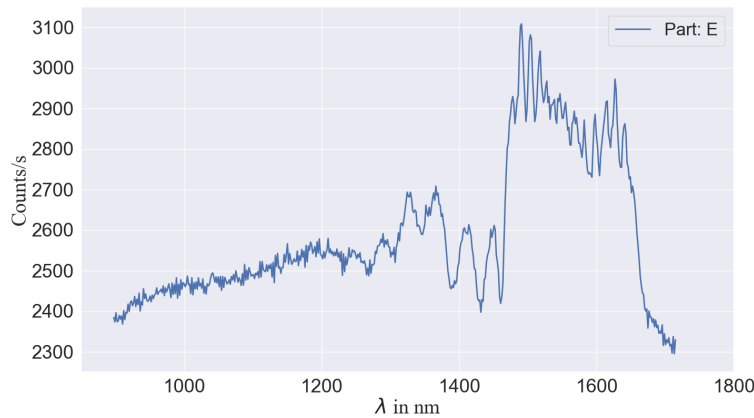


Figure A.1.6: Shows the reflected spectra from part E of sample 8366. See figure 3.2.2b for the setup.

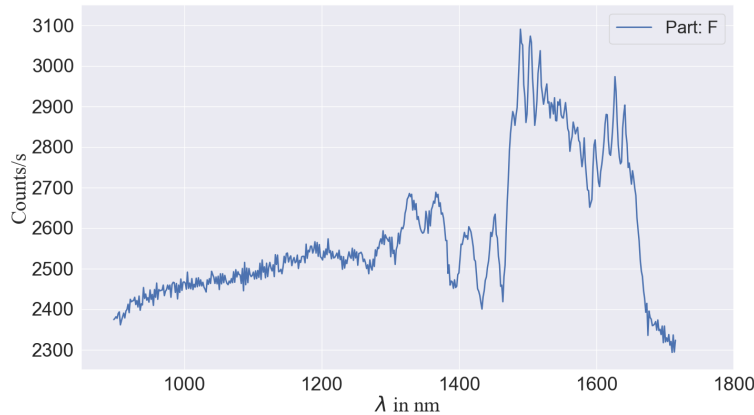


Figure A.1.7: Shows the reflected spectra from part F of sample 8366. See figure 3.2.2b for the setup.

APPENDIX A. ADDITIONAL PLOTS

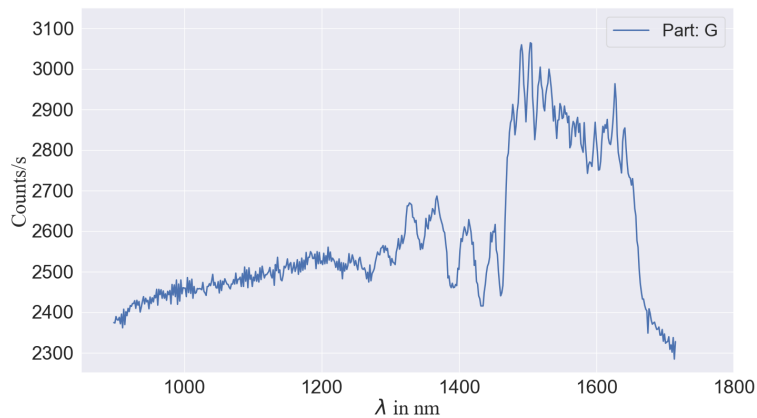


Figure A.1.8: Shows the reflected spectra from part G of sample 8366. See figure 3.2.2b for the setup.

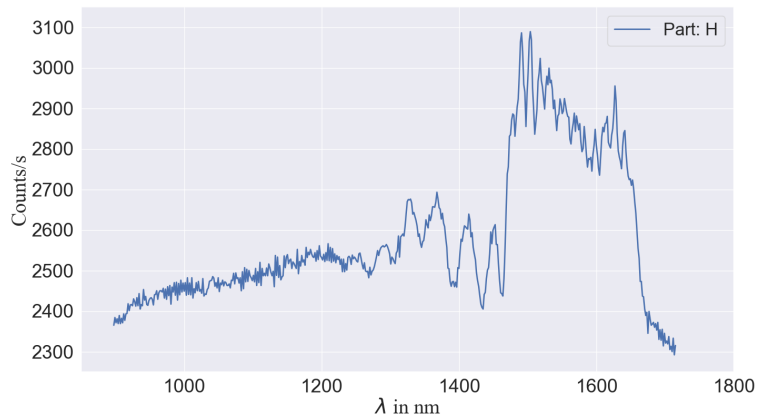


Figure A.1.9: Shows the reflected spectra from part H of sample 8366. See figure 3.2.2b for the setup.

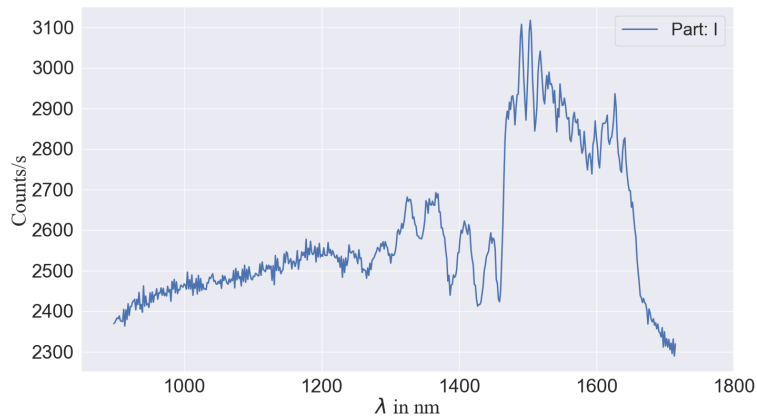


Figure A.1.10: Shows the reflected spectra from part I of sample 8366. See figure 3.2.2b for the setup.

APPENDIX A. ADDITIONAL PLOTS

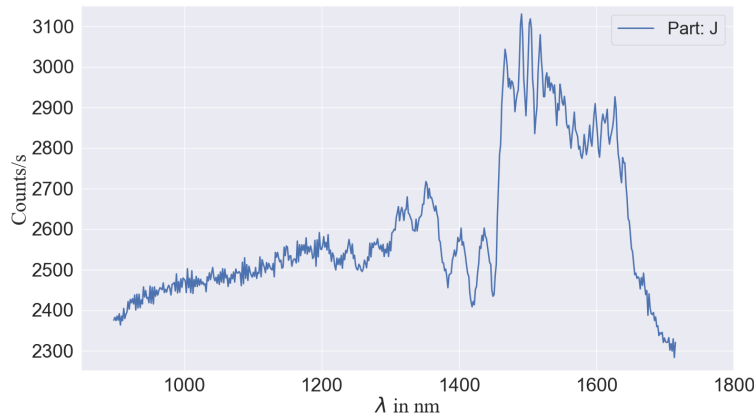


Figure A.1.11: Shows the reflected spectra from part J of sample 8366. See figure 3.2.2b for the setup.

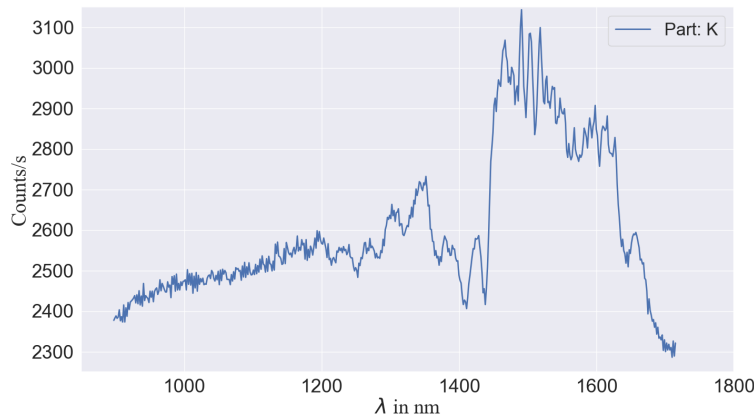


Figure A.1.12: Shows the reflected spectra from part K of sample 8366. See figure 3.2.2b for the setup.

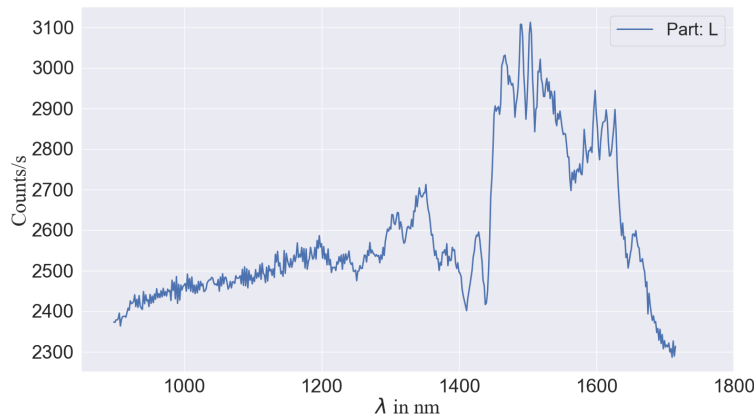


Figure A.1.13: Shows the reflected spectra from part L of sample 8366. See figure 3.2.2b for the setup.

APPENDIX A. ADDITIONAL PLOTS

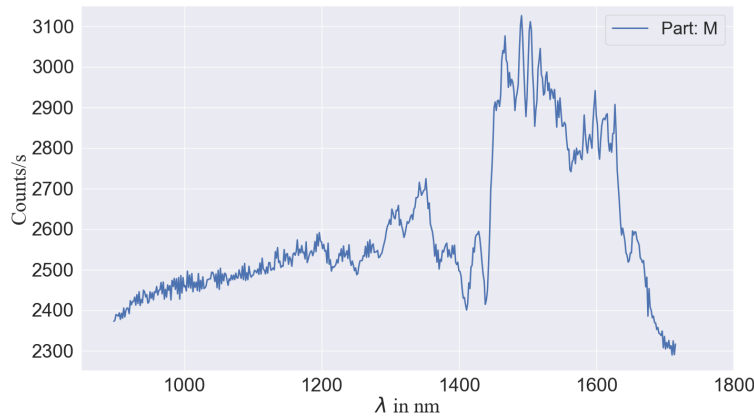


Figure A.1.14: Shows the reflected spectra from part M of sample 8366. See figure 3.2.2b for the setup.

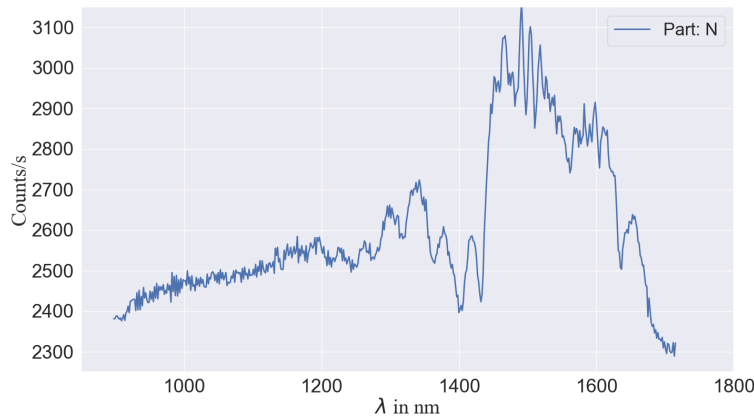


Figure A.1.15: Shows the reflected spectra from part N of sample 8366. See figure 3.2.2b for the setup.

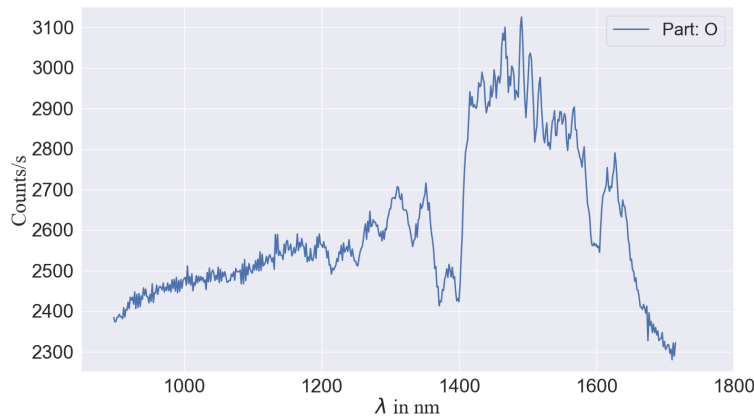


Figure A.1.16: Shows the reflected spectra from part O of sample 8366. See figure 3.2.2b for the setup.

APPENDIX A. ADDITIONAL PLOTS

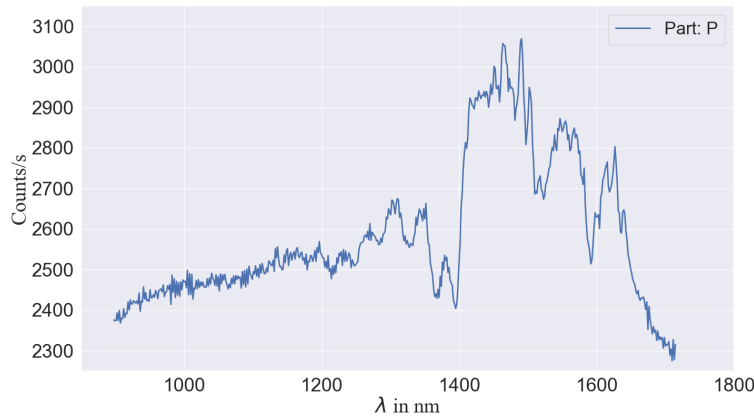


Figure A.1.17: Shows the reflected spectra from part P of sample 8366. See figure 3.2.2b for the setup.

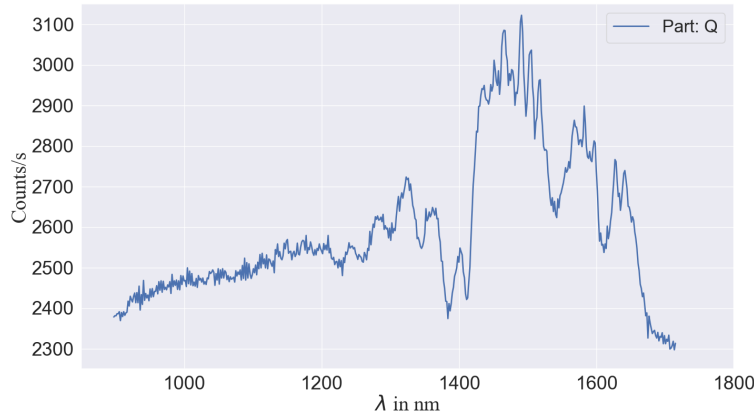


Figure A.1.18: Shows the reflected spectra from part Q of sample 8366. See figure 3.2.2b for the setup.

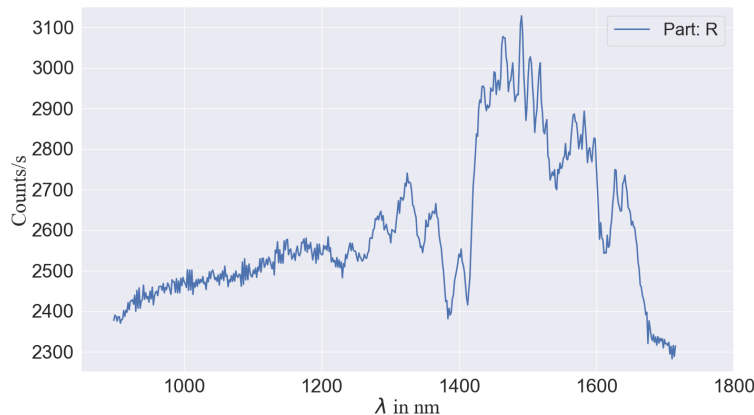


Figure A.1.19: Shows the reflected spectra from part R of sample 8366. See figure 3.2.2b for the setup.

A.2 Quantum Dot Characterization

Here the full spectra from the QD is shown for the polarization series as well as a more zoomed in version. The peak fitted energy oscillations for the X and XX are also shown in figure A.2.3 and A.2.4.

A.2.1 Polarization Series and FSS

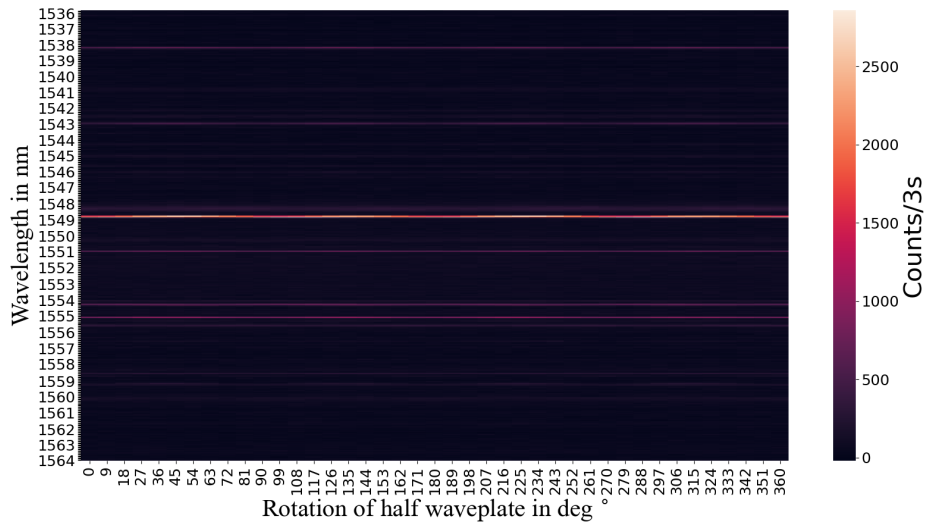


Figure A.2.1: Shows the full emission spectra from the QD during the polarization series done in subsection 3.2.2.

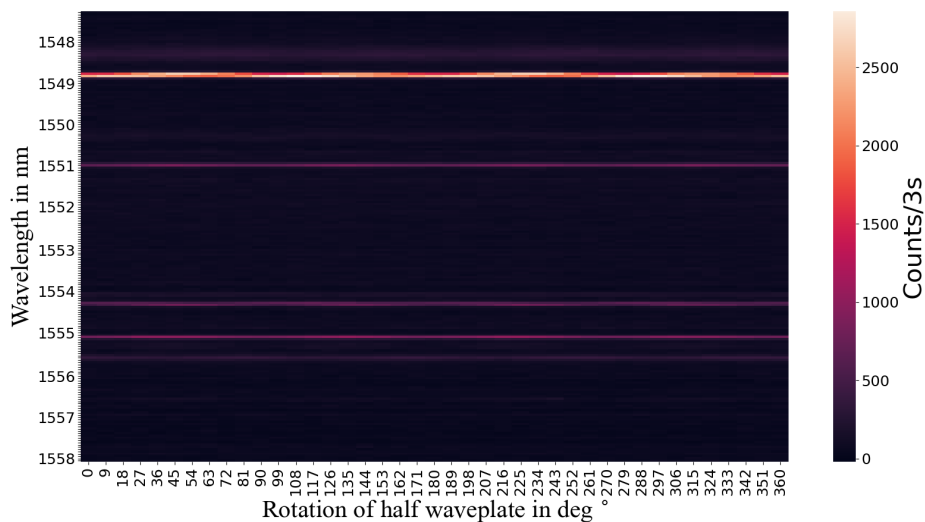


Figure A.2.2: Shows a more zoomed in version of the emission spectra from the QD during the polarization series done in subsection 3.2.2.

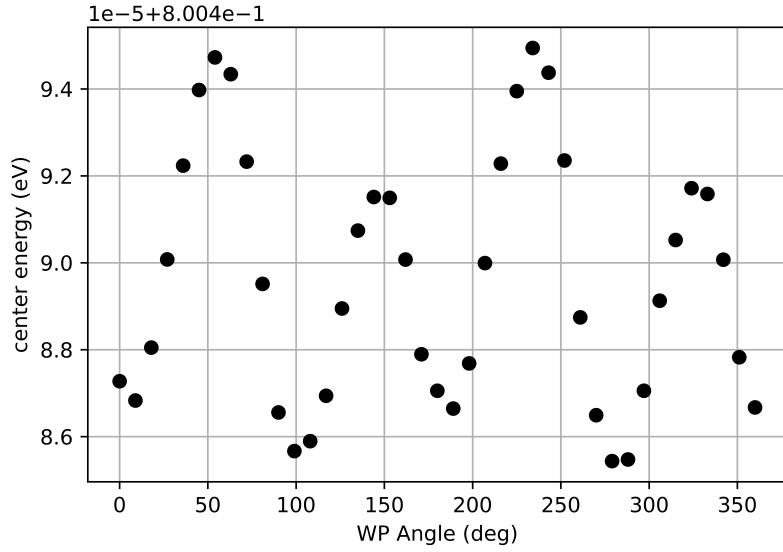


Figure A.2.3: Shows the energy oscillation for the X emission during the polarization series done in subsection 3.2.2. Amplitude $3.7101e - 06 \pm 2.6566e - 07$ with a fitting error of 7.16%.

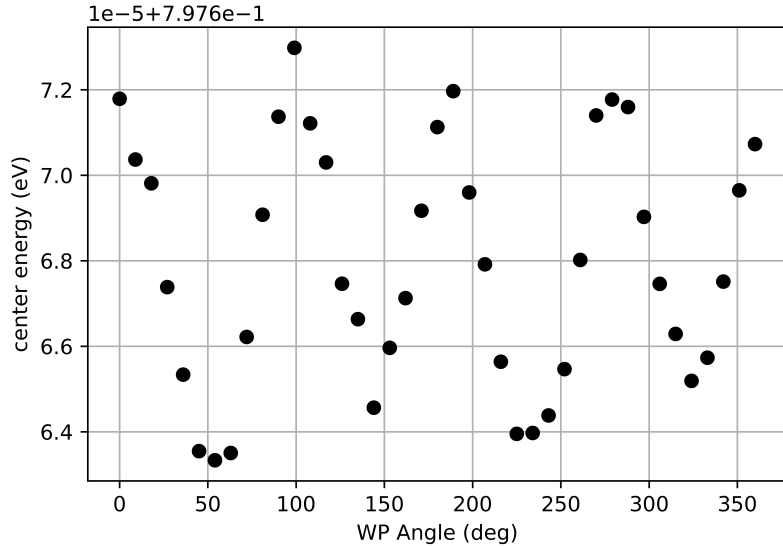


Figure A.2.4: Shows the energy oscillation for the XX emission during the polarization series done in subsection 3.2.2. Amplitude $3.7751e - 06$ with a fitting error of $2.0479e - 07$, 5.42%

A.2.2 Power series

In figure A.2.5, the power series for the full spectra of the QD is shown.

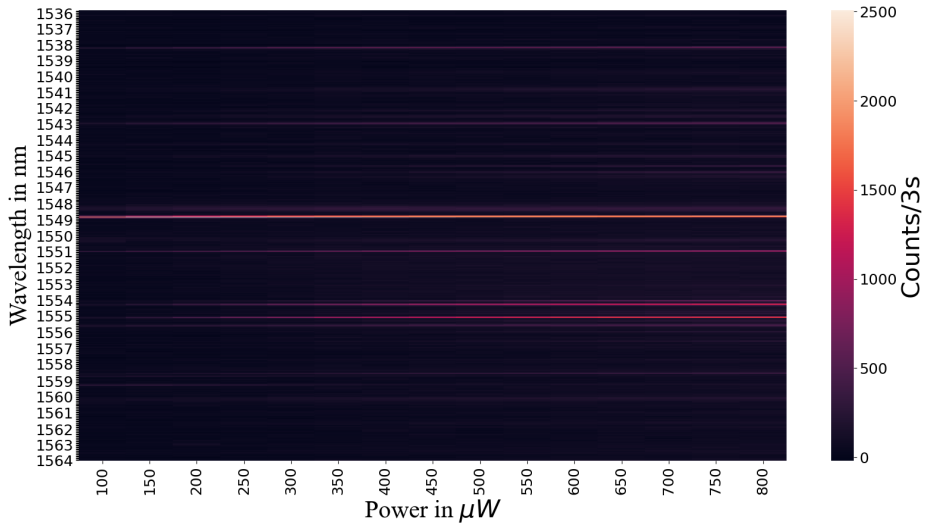


Figure A.2.5: Shows the full emission spectra from the QD during the power series measurement done in subsection 3.2.2. Here the values shown on the x-axis come from the powermeter and the actual excitation power is 1/9 of the given values as the powermeter receives 90% of the laser light and the QD receives 10%. See figure 3.2.4a for setup.

A.2.3 Lifetime of the Exciton

Here the plot used to estimate the lifetime of the X from the zero peak of the single QuTag measurement in the cascade histogram 4.3.2 is shown.

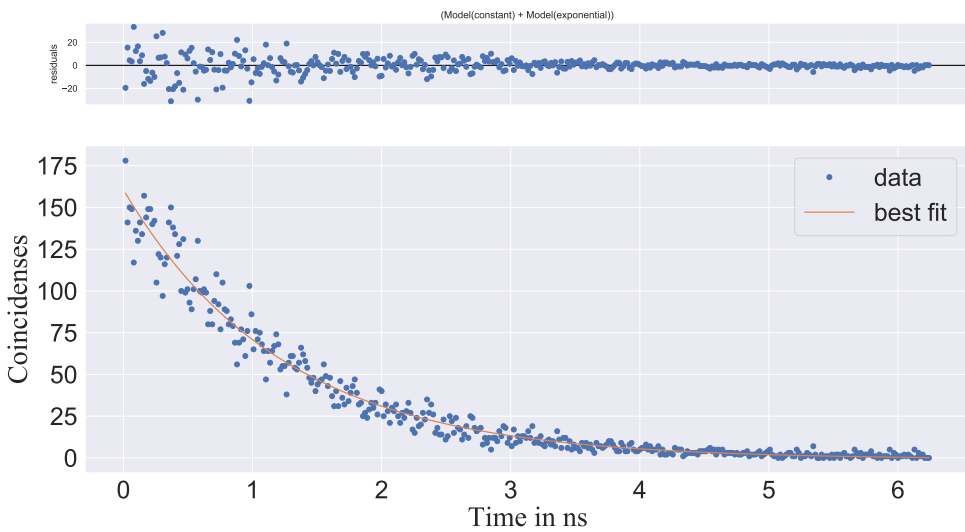


Figure A.2.6: Shows the lm fit plot for the X lifetime approximated from the cascade histogram. A lifetime of 1.23 ns was found when using a binsize of 16 ps.

Appendix B

ETA Graphs and Code

In this section the graphical *state diagrams* of ETA is shown, including the code needed for them to work, see figures B.1.1, B.1.2 and B.1.3. ETA state diagrams as well as the code used for synchronization of the two time-tagger are presented here. The rest of the code needed is provided by premade scripts. For additional information look at <https://eta.readthedocs.io/en/latest/>.

B.1 State Diagrams and ETA Code

B.1.1 How to read in a data file in ETA

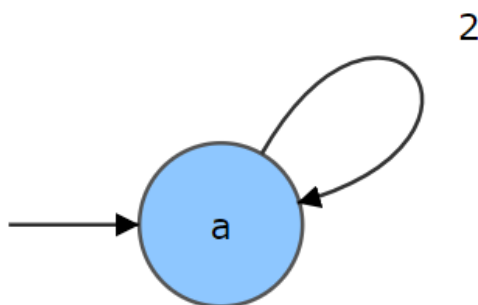


Figure B.1.1: Firstly the data is loaded in as illustrated by the right arrow furthest to the left. Delays the 2 input channel by 'fw-delay' ps to a new virtual channel 21, see code below.

ETA code belonging to the delay state diagram in figure B.1.1

a :

```
emit(21, 'fw-delay')
```

B.1.2 How the g^2 histogram is created using ETA

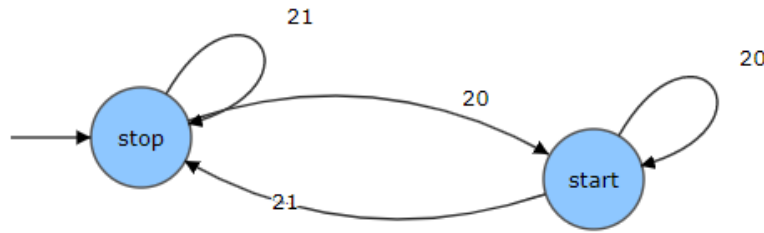


Figure B.1.2: Firstly the data is loaded in as illustrated by the right arrow furthest to the left. A clock is stated given an even on channel 20 and stops it if the next detection event is on channel 21. If the subsequent detection event is on channel 20 the clock is restarted. Given an event on channel 20 followed by two subsequent events on channel 21 both detection events are recorded and stored.

ETA code belonging to the g^2 -state diagram in figure B.1.2.

```
HISTOGRAM(h4,( 'bins ', 'binsize '))
HISTOGRAM(h4_zero ,(1 ,1))
CLOCK(c4,100,1)
start:
    c4.start()
stop:
    c4.stop()
    h4.record_all(c4)
    h4_zero.record_all(c4)
```

B.1.3 How the cascade histogram is created using ETA

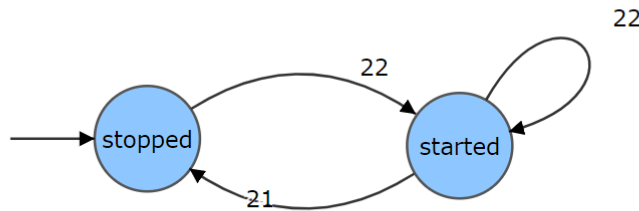


Figure B.1.3: Firstly the data is loaded in as illustrated by the right arrow furthest to the left. A clock is stated given an event on channel 22 and stops it if the next detection event is on channel 21. If the subsequent detection event is on channel 22 the clock is restarted. Given an event on channel 22 followed by two subsequent events on channel 21 only the first event on channel 21 would be recorded and stored.

ETA code belonging to the cascade state diagram in figure B.1.3

```
CLOCK(c3)  
HISTOGRAM(t3 ,('bins','binsize'))
```

```
started:  
    c3.start()  
stopped:  
    c3.stop()  
    t3.record(c3)
```

B.2 ETA Synchronization Code

Code used to correct the offset for the two qutags, read in two files to ETA and synchronize the two files.

To read in two data files into ETA

```
# Analyze files loaded in both timetaggers  
from pathlib import Path
```

```
#-----ETA PROCESSING-----
fp_1 = Path(file1)
fp_2 = Path(file2)

cut_1 = eta.clip_file(fp_1, read_events=1)
result_1 = eta.run({"setup_tt": cut_1}, group='setup',
return_results=True, max_autofeed=1)

cut_2 = eta.clip_file(fp_2, read_events=1)
result_2 = eta.run({"setup_tt": cut_2}, group='setup',
return_results=True, max_autofeed=1)

offset_1 = result_1["starttime"]
offset_2 = result_2["starttime"]

eta.recipe.set_parameter("offset1_ps", str(offset_1))
eta.recipe.set_parameter("offset2_ps", str(offset_2))
eta.load_recipe()

eta.send(f"Offset{file1}{offset_1}ps")
eta.send(f"Offset{file2}{offset_2}ps")
```

To synchronize the two data files

```
# Analyze files loaded in both time-taggers
from pathlib import Path

#-----ETA PROCESSING-----
fp_1 = Path(file1)
fp_2 = Path(file2)

cut_1 = eta.clip_file(fp_1, read_events=1)
result_1 = eta.run({"setup_tt": cut_1}, group='setup',
                   return_results=True, max_autofeed=1)

cut_2 = eta.clip_file(fp_2, read_events=1)
result_2 = eta.run({"setup_tt": cut_2}, group='setup',
                   return_results=True, max_autofeed=1)

offset_1 = result_1["starttime"]
offset_2 = result_2["starttime"]

eta.recipe.set_parameter("offset1_ps", str(offset_1))
eta.recipe.set_parameter("offset2_ps", str(offset_2))
eta.load_recipe()

eta.send(f"Offset{file1}{offset_1}ps")
eta.send(f"Offset{file2}{offset_2}ps")
```

Code used for the synchronization of the two qutags.

```
import numpy as np
import pandas as pd
from pathlib import Path
import os

import etabackend.tk.plot as etapl
import etabackend.tk.utils as etautils
```

```
from scipy.io.wavfile import write
from scipy.fft import fft, fftfreq, rfft, rfftfreq, irfft

#-----ADJUST DELAY-----
delay = int(float(delay)) # Upper boundary of magnitude
bins = int(float(bins))
binsize = int(float(binsize))
offset_1_ps = int(offset1_ps)
offset_2_ps = int(offset2_ps)
ratio = int(float(ratio)) #
finalstepsize = int(float(finalstepsize))

def setDelay(delay):
    """Set the delay for the cascade"""
    eta.recipe.set_parameter("bw_delay", str(max(0, -1*delay)))
    eta.recipe.set_parameter("fw_delay", str(max(0, delay)))
    eta.load_recipe()

def process():
    """Returns the cascade histogram as well as the x-axis"""
    cut_1 = eta.clip_file(fp_1, read_events=1)
    cut_1.GlobalTimeShift = -offset_1_ps

    cut_2 = eta.clip_file(fp_2, read_events=1)
    cut_2.GlobalTimeShift = -offset_2_ps

    cut_1 = eta.clips(fp_1, modify_clip=cut_1)
    cut_2 = eta.clips(fp_2, modify_clip=cut_2)

    result = eta.run({"timetagger1": cut_1, "timetagger2": cut_2},
                     group='experiment')
```

```
fullhist=result[ 't3 ']
xdata = np.arange(fullhist.size) * binsize
return fullhist , xdata

----- Starting Delay -----
setDelay(delay)
fp_1 = Path(file1)
fp_2 = Path(file2)
DATAFOLDER = 'analyzed\data'

f=Path(fp_1)
print(fp_1.stat().st_mtime)
print(fp_2.stat().st_mtime)

def FT(delay_ft):
    """
    Returns the amplitude of the Fourier Transform
    cascade histogram at 80MHz frequency
    """
    setDelay(int(delay_ft))
    #fullhist , xdata = process()
    fullhist , _ = process() #ignores the second output
                            #from the process function

    Sample_rate = 10**8 # Need more than 80 MHz so we go with 100MHz
    Total_time = bins * binsize # Measured in ps
    Samples = int(Total_time * 10**-12 * Sample_rate)
    # 10**-12 is to make sure the units check out
    FThist = rfft(fullhist)
    FTx = rfftfreq(Samples, 1 / Sample_rate)
    # Allocates too much memory, trying to find a work around
```

```
# The maximum frequency is half the sample rate
points_per_freq = len(FTx) / (Sample_rate / 2)
target_index = int(points_per_freq * 8 * 10**7)
return np.abs(FThist[target_index])

def maximize(start, ratio):
    """
    Maximizes the amplitude of the 80MHz frequency amplitude
    of the Fourier Transformed cascade histogram down
    to the final stepsize with the ratio decrease in stepsize
    and returns the final delay to achieve synchronization!
    """
    final_delay = 0
    stepsize = start
    while stepsize >= finalstepsize:
        amplist = [FT(final_delay + stepsize * i) \\
                   for i in range(-ratio, ratio + 1)]
        final_delay += (amplist.index(np.max(amplist)) * stepsize)
        stepsize = stepsize / ratio
    return final_delay

sync = maximize(delay, ratio)
setDelay(int(sync))
bins = bins * ratio**2 # Trying to find the maximum peak from here on

fullhist, _ = process()
# Now finding the zero peak! Find the maximum of
# the histogram and add/subtract the maximum_index * binsize
index_of_maximum = np.argmax(fullhist)
zero_peak = index_of_maximum * binsize
sync -= zero_peak
setDelay(int(sync))
```

```
fullhist , xdata = process()

LABEL = "Cascade□with□max□" + str(fullhist.max())
-----PLOTTING-----

df = pd.DataFrame(np.vstack((xdata, fullhist)).T,
                  columns=[ 'time□bins' , 'histogram□events' ])
df[ 'log□events' ] = np.clip(df[ 'histogram□events' ].values , 0.5 , None)

def generate_doc(doc):
    root = etaplt.plot_histogram(df, f,
        f.parent.joinpath(DATAFOLDER),
        data_name=LABEL.capitalize(), file_label=LABEL.lower(),
        info=etautils.info(globals_dict=eta.compilecache_vars[ 'experiment' ],
                           recipe_type=LABEL))
    doc.add_root(root)
return doc

eta.display(generate_doc, 'bokeh')
```